The FIGNL1-FIRRM complex is required to complete meiotic recombination in the mouse and prevents massive DNA damage-independent RAD51 and DMC1 loading

Akbar Zainu[1], Pauline Dupaigne[2], Soumya Bouchouika[1,3], Julien Cau[4], Julie A. J. Clément[5], Pauline Auffret[1,6], Virginie Ropars[7], Jean-Baptiste Charbonnier[7], Bernard de Massy[1], Rajeev Kumar[8], Frédéric Baudat[9]

[1] Institut de Génétique Humaine, University of Montpellier, CNRS, Montpellier, France.

[2] Genome Integrity and Cancers UMR9019 CNRS, Université Paris- Saclay, Gustave Roussy, F-94805 Villejuif Cedex, France.

[3] Present address: Institut de Génétique Moléculaire de Montpellier, CNRS-UMR 5535, Univ Montpellier, Montpellier, France.

[4] Biocampus Montpellier, University of Montpellier, CNRS, INSERM, Montpellier, France

[5] IHPE, Univ Montpellier, CNRS, IFREMER, Univ Perpignan Via Domitia, Perpignan, France

[6] Present address: Ifremer, IRSI, Service de Bioinformatique (SeBiMER), Plouzané, France.

[7] Institute for Integrative Biology of the Cell (I2BC), Université Paris-Saclay, CEA, CNRS, Gif-sur-Yvette, France.

[8] Institut Jean-Pierre Bourgin, INRA, AgroParisTech, CNRS, Université Paris-Saclay, 78000 Versailles, France.

[9] Institut de Génétique Humaine, University of Montpellier, CNRS, Montpellier, France.

frederic.baudat@igh.cnrs.fr

Running title: FIGNL1-FIRRM in mouse meiosis

Keywords: meiosis; homologous recombination; FIGNL1; FIRRM; RAD51; DMC1

Abstract

During meiosis, nucleoprotein filaments of the strand exchange proteins RAD51 and DMC1 are crucial for repairing SPO11-generated DNA double-strand breaks (DSBs) by homologous recombination (HR). A balanced activity of positive and negative RAD51/DMC1 regulators ensures proper recombination. Fidgetin-like 1 (FIGNL1) was previously shown to negatively regulates RAD51 in human cells. However, FIGNL1's role during meiotic recombination in mammals remains unknown. Here, we deciphered the meiotic functions of FIGNL1 and of FIGNL1 interacting regulator of recombination and mitosis (FIRRM) using male germline-specific conditional knock-out (cKO) mouse models. Both FIGNL1 and FIRRM are required for completing meiotic prophase in mouse spermatocytes. Despite efficient recruitment of DMC1 on ssDNA at meiotic DSB hotspots, the formation of late recombination intermediates is defective in *Firrm* cKO and *Fignl1* cKO spermatocytes. Moreover, the FIGNL1-FIRRM complex limits RAD51 and DMC1 accumulation on intact chromatin, independently from the formation of SPO11-catalyzed DSBs. Purified human FIGNL1ΔN alters the RAD51/DMC1 nucleoprotein filament structure and inhibits strand invasion *in vitro*. Thus, this complex might regulate RAD51 and DMC1 association at sites of meiotic DSBs to promote proficient strand invasion and processing of recombination intermediates.

Introduction

Meiosis ensures the accurate reduction of chromosome numbers in gametes during sexual reproduction. Erroneous meiosis results in sterility or fertility defects owing to aberrant gametes formation. During meiosis, homologous chromosomes (homologs) undergo pairing, synapsis, and recombination. Homologous recombination (HR) is crucial for crossover (CO) formation between homologs to ensure their balanced segregation during meiosis, and for promoting pairing and synapsis of homologs in some organisms including mammals [1–3]. HR is initiated by genome-wide SPO11-dependent DNA double-strand breaks (DSBs) formation [4]. SPO11 is subsequently released from DSB sites as SPO11-oligonucleotide complex by resection machinery giving rise to 3' single-stranded DNA (ssDNA) overhangs [5,6]. The heterotrimeric complex of Replication Protein A (RPA) binds to and protects the ssDNA overhangs from nucleolytic degradation. Two eukaryotic RecA-like strand-exchange proteins, RAD51 and its meiosis-specific paralog DMC1, replace RPA on ssDNA with the help of the mediator protein BRCA2 [7,8]. Both strand exchange proteins can catalyze homology search and strand exchange through invasion on an intact template, leading to formation of a joint molecule termed

displacement loop (D-loop) [9]. The invading end primes DNA synthesis that requires the dissociation of RAD51/DMC1 from double-strand DNA (dsDNA) within the D-loop. After D-loop formation, meiotic DSB repair can produce a non-crossover (NCO), or a CO by two alternative pathways that coexist in many organisms [2]. In mice, the meiosis-specific class I CO pathway generates 90% of COs and is dependent on a set of proteins referred to as ZMM proteins (including the MSH4-MSH5 complex and TEX11) [10,11] and the MutL homologs MLH1-MLH3. Mouse MSH4 and MSH5 are essential to repair most if not all meiotic DSBs [2,12–14]. The class II COs (~10% of COs in the mouse) depend on structure-specific endonucleases [2].

Both RAD51 and DMC1 form foci colocalizing extensively at DSB sites [15,16] and are proposed to assemble into side-by-side homo-filaments on ssDNA tails, with RAD51 at the DSB-distal region and DMC1 polymerizing on the 3', DSB-proximal region [9,17,18]. DMC1 is likely the main catalyzer of meiotic interhomolog recombination in most eukaryotes, while RAD51 plays crucial non-catalytic accessory roles [18–20]. RAD51 is the sole strand exchange protein during mitotic recombination and also plays a strand exchange activity-independent role in the replication fork protection that might rely on its dsDNA-binding capacity [21–26]. Besides this specific function, inactive filaments of RAD51 and DMC1 on dsDNA are likely toxic and are actively prevented [27]. Members of the Swi2/Snf2-related RAD54 translocase family [28] prevent the accumulation of RAD51 on dsDNA in human cells [29], and of Rad51 and Dmc1 in *S. cerevisiae* [30,31]. In *S. cerevisiae*, Rad54 and its paralog Rdh54 promote strand invasion, and remove RAD51/DMC1 from dsDNA following D-loop formation [28,32]. In mouse, RAD54 and its paralog RAD54B are not essential for meiotic recombination, because the *Rad54 Rad54b* double mutant mice are fertile [33,34]. Many proteins regulate RAD51/DMC1 nucleofilament formation positively and negatively. Positive factors are required to form stable and active RAD51-ssDNA filaments [7,8]. One of them is the Shu complex that comprises in mammals the distant RAD51 paralog SWSAP1, the SWIM-domain containing SWS1 and SPIDR [35–39]. It promotes the formation of stable RAD51 filaments and HR associated with replication, is important for assembling stable RAD51 and DMC1 filaments during meiotic recombination in the mouse, but is not essential for viability [36,37,40–42]. The SWSAP1-SWS1-SPIDR complex might promote specifically the stable assembly of longer RAD51 nucleoprotein filaments involved in some HR types, especially interhomolog HR [36,37].

FIGNL1 (fidgetin-like 1) forms an evolutionary conserved complex with FIRRM (FIGNL1 interacting regulator of recombination and mitosis) that interacts with RAD51 and DMC1 [43–46]. In Arabidopsis and rice meiosis, FIGNL1 and FIRRM homologs regulate negatively the dynamics of RAD51 and DMC1 foci and limit the formation of class II crossovers [44,45,47–49]. Arabidopsis *figl1* (*Figl1* homolog) and *flip* (*Firrm* homolog) mutants are fertile with all meiotic DSBs repaired [44,47,50]. Conversely, unrepaired DSBs persist in rice *fignl1* and *meica* (*Firrm* homolog) mutants, leading to chromosome fragmentation and sterility [48,49]. The regulation of RAD51/DMC1 focus formation in Arabidopsis somatic and meiotic cells involves

an antagonistic interplay between BRCA2 and FIGL1, consistent with FIGL1 acting as a negative regulator of RAD51/DMC1 filament [51]. In human cells, a similar antagonistic mechanism was found between the SWSAP1-SWS1-SPIDR complex and FIGNL1, which interacts with SWSAP1 [41] and SPIDR [43]. Indeed, FIGNL1 depletion relieves the dependency on SWSAP1 and SWS1 for forming RAD51 repair foci [41]. Moreover, purified human SWSAP1 protects RAD51-ssDNA filament from dissociation promoted by FIGNL1 *in vitro* [41]. However, the role of FIGNL1 and FIRRM remains unknown during meiotic recombination in mammals.

In this study, we investigated the role of the FIGNL1-FIRRM complex in meiotic recombination by analyzing germ line-specific mouse conditional knock-out models for both genes. The depletion of FIGNL1 or FIRRM in mouse spermatocytes results in meiotic DSB repair failure and no full synapsis between homologs during meiotic prophase I, leading to prophase I arrest and apoptosis. Surprisingly, *Fignl1* cKO and *Firrm* cKO spermatocytes also show an abundant DSB-independent accumulation of RAD51 and DMC1 on chromatin and meiotic chromosome axes during premeiotic replication and early meiotic prophase stages. This indicates that the FIGNL1-FIRRM complex prevents the formation of stable inactive RAD51 and DMC1 filament, presumably on intact dsDNA, in mouse spermatocyte nuclei.

Results

FIGNL1 and FIRRM are required for meiotic prophase completion in the mouse male germline

We wanted to determine the roles of FIGNL1 and its putative partner FIRRM (also called BC055324) during meiosis. As both genes are essential for mouse viability (IMPC, https://www.mousephenotype.org/), we generated cKO lines with Cre expression under the control of the *Stra8* promoter [52] to ablate *Firrm* or/and *Fignl1* in the male germline shortly before meiosis onset (*Firrm* cKO and *Fignl1* cKO, Extended Data Fig. 1a-b). Testis weight was similarly reduced in *Firrm* cKO, *Fignl1* cKO, and *Firrm-Fignl1* double cKO mice compared with wild-type controls (Fig. 1a). Analysis of testis sections from adult *Firrm* cKO and *Fignl1* cKO animals showed the presence of seminiferous tubules with Sertoli cells, spermatogonia and spermatocytes, but absence of haploid cells (spermatids), suggesting a prophase I arrest (Fig. 1b). The presence of some tubules with a small number of round spermatids and of few tubules with many round and elongated spermatids, like in controls, suggested incomplete Cre-mediated excision, as described in other conditional mouse mutants obtained with this *Stra8-Cre* transgene [53–55]. In testes from 12-day post-partum (12 dpp) *Firrm* cKO and *Fignl1* cKO mice, FIRRM and FIGNL1 protein expression levels in the cytoplasmic and nuclear fractions were greatly and

similarly reduced compared to controls (Fig. 1c). This suggests that they reciprocally regulate their stability, which is consistent with forming a complex. The residual protein level might result from expression in non-meiotic cells (spermatogonia or somatic cells) and/or from incomplete Cre-induced gene deletion in a fraction of spermatocytes (see above). Conversely, RAD51 expression in the nuclear fraction was increased in *Firrm* cKO and *Fignl1* cKO testes, suggesting that the FIGNL1-FIRRM complex might be implicated in limiting directly or indirectly nuclear accumulation of RAD51 (but not of DMC1). This might have significant consequences, because RAD51 nuclear level is suggested play a role in HR regulation [56].

The synaptonemal complex (SC), a tripartite proteinaceous structure, links the axes of homologous chromosomes during meiotic prophase. To analyze if synapsis was impaired in *Firrm* cKO and *Fignl1* cKO, we stained surface-spread spermatocyte nuclei with antibodies against SYCP3, a component of meiotic chromosome axes, and SYCP1, a protein of the SC central element (Fig. 1d). *Firrm* cKO and *Fignl1* cKO spermatocytes formed apparently normal meiotic chromosome axes (leptotene stage), suggesting a normal meiotic prophase entry. However, most nuclei showed unsynapsed or partially synapsed axes, indicating accumulation of zygotene-like cells. The small fraction of *Fignl1* cKO and *Firrm* cKO spermatocytes that progressed toward normal-looking pachytene with all chromosomes pairs fully synapsed and diplotene with desynapsed chromosomes might be explained by incomplete Cre-mediated excision in these cells (Fig. 1e). We followed prophase I progression during the first wave of meiosis in *Firrm* cKO, from 12 dpp to 18 dpp. We detected a deficit in more advanced stages already in 12 dpp *Firrm* cKO spermatocytes. At 16 and 18 dpp, most nuclei were arrested at a zygotene-like stage, and the percentage of nuclei at the pachytene and diplotene stages was strongly reduced (at 18 dpp, 78% of control versus 15% of *Firrm* cKO nuclei). Approximately 30% of *Firrm* cKO prophase I nuclei displayed an abnormal zygotene/pachytene-like pattern, with non-homologous synapsis and only few synapsed chromosome axes (Fig. 1d, middle panel). These findings in 12 dpp to 18 dpp spermatocytes are suggestive of an arrest in early pachytene and a defect in homologous synapsis. Adult *Fignl1* cKO animals displayed a similar deficit in pachytene-diplotene spermatocytes (Fig. 1e), consistent with the hypothesis that FIGNL1 and FIRRM act together.

The formation and initial processing of meiotic DSBs are unaffected in *Firrm* cKO and *Fignl1* cKO spermatocytes

This synapsis defect associated with a mid-prophase arrest might result from defective recombination initiation (e.g. *Spo11*$^{-/-}$ [57,58]) or defective repair of meiotic DSBs (e.g. *Dmc1*$^{-/-}$ [59,60]) [3]. To determine whether DSB formation was altered by FIRRM or FIGNL1 depletion, we quantified phosphorylated H2AX (γH2AX) that decorates chromatin in a DSB-specific manner at leptotene [61]. The γH2AX signal

intensity in the nucleus was not different in control and *Firrm* cKO spermatocytes from pre-leptotene (stage of pre-meiotic replication) to leptotene (Fig. 2a-b). RPA2, a subunit of RPA, is involved in DNA replication and HR and forms multiple foci at replication forks in preleptotene spermatocytes, and along chromosome axes at sites of recombination intermediates from leptonema to pachynema [53,62,63]. RPA2 foci displayed the same kinetics in *Firrm* cKO, *Fignl1* cKO, and control spermatocytes (Fig. 2c-d), except for a trend toward an increase in early zygonema (by 1.3- and 1.4-fold for *Firrm* cKO and *Fignl1* cKO, respectively). Thus, the first steps of meiotic recombination (DSB formation and RPA recruitment on resected ssDNA ends) were not affected by the absence of the FIGNL1-FIRRM complex.

The recruitment of RAD51 and DMC1 on meiotic chromatin strongly increases in the absence of FIGNL1 or FIRRM

In mouse spermatocytes, RAD51 and DMC1 foci extensively colocalize on meiotic chromosome axes (on-axis foci) from leptotene to pachytene stage, particularly in zygotene [15,16,62]. Compared with controls, RAD51 and DMC1 signal intensity and foci pattern and kinetics were strikingly different in *Firrm* cKO and *Fignl1* cKO spermatocytes (Fig. 3a-c; Extended Data Fig. 2a). First, RAD51 (but not DMC1) formed many foci at preleptotene, during premeiotic replication. Second, the mean number of RAD51 and DMC1 on-axis foci was significantly higher in *Firrm* cKO and *Fignl1* cKO than in control spermatocytes at every stage, from early leptotene to zygotene. Third, in cKO spermatocytes, many RAD51 and DMC1 foci were located away from the chromosome axes (off-axis foci). The number of off-axis foci was highest during leptotene and progressively decreased during zygotene. Fourth, in cKO spermatocytes, RAD51 and DMC1 staining formed continuous lines, at our resolution limit, along the synaptonemal complex segments in zygotene-like nuclei. This did not allow counting RAD51 and DMC1 foci in late zygotene-like nuclei with extensive synapsis. Overall, these observations are consistent with a role of FIRRM and FIGNL1 in limiting RAD51 and DMC1 loading on chromatin in spermatocyte nuclei. We describe these different features in the following sections.

Post-strand invasion recombination foci are strongly reduced in the absence of FIRRM

The efficient recruitment of RAD51 and DMC1 prompted us to examine MSH4 and TEX11, two meiotic stabilizing post-strand invasion recombination intermediate ZMM proteins [11], which form foci on SC from zygotene to mid-pachytene [3,62,64]. The number of MSH4 and TEX11 foci was strongly reduced in late zygotene-like *Firrm* cKO nuclei compared with control (Fig. 3d, Extended Data Fig. 2b). To normalize differences in SC extension among genotypes, we measured the density of MSH4 foci per µm of SC length. MSH4 focus density was reduced by 2.5-fold in *Firrm* cKO compared with control spermatocytes (Fig. 3e, Extended Data Fig. 2c), although the number of MSH4 foci was higher than in *Spo11*$^{YF/YF}$ nuclei (without DSB-inducing activity). Thus, FIRRM is required for TEX11 and MSH4 focus

formation during mouse meiotic recombination. The residual MSH4 foci might result from MSH4 binding to a small fraction of normal or aberrant recombination intermediates formed in the absence of the FIGNL1-FIRRM complex. Alternatively, we cannot exclude the persistence of a small amount of FIRRM protein in *Firrm* cKO spermatocytes, sufficient for recruiting MSH4 to few recombination intermediates. Thus, despite the increased recruitment of RAD51 and DMC1 on chromosome axes, the processing of recombination intermediates was defective in *Firrm* cKO spermatocytes, suggesting a function of FIGNL1-FIRRM at a step likely before recombination intermediate stabilization by MSH4-MSH5.

In *Firrm* cKO and *Fignl1* cKO preleptotene spermatocytes, RAD51 is recruited on chromatin during premeiotic replication

RPA2 forms many foci at ongoing replication forks in preleptotene nuclei (Fig. 3f-g). The kinetics of RPA2 focus formation was similar in control, *Firrm* cKO and *Fignl1* cKO spermatocytes, and few foci remained in early leptotene stage. This suggests that premeiotic replication was completed without major alteration (Fig. 2d; Extended Data Fig. 2d). As RAD51 is involved in protecting stalled replication forks [65], we hypothesized that RAD51 might colocalize with RPA during premeiotic replication in *Firrm* cKO and *Fignl1* cKO spermatocytes. We measured the colocalization of RAD51 and RPA2 in preleptotene spermatocytes and compared these data with the colocalization of randomly distributed foci obtained from simulations (see Methods; Fig. 3h-i; Extended Data Fig. 2e). In *Fignl1* cKO, 17% of RAD51 foci colocalized with RPA2 foci compared with 9% of randomly generated RAD51 foci ($p < 0.0001$; two-tailed Wilcoxon test), suggesting that a fraction of RAD51 foci localizes at replication forks. However, the majority of identified RAD51 foci was not coincided with RPA2 foci, suggesting that a larger fraction of RAD51 foci may not localize at replication forks. We cannot exclude that both RAD51 and RPA localize at forks in an exclusive manner, and that RAD51 binding excludes RPA. However, because of the large number of RAD51 foci that persisted at the end of premeiotic replication and the absence of obvious gross replication defects, we hypothesize that RAD51 colocalizes transiently with RPA at replication forks. It then remains in place, likely on intact DNA, while the forks progress and move away. DMC1 foci were rare in most *Firrm* cKO and *Fignl1* cKO preleptotene spermatocytes (Fig. 3c), likely because meiosis-specific DMC1 production is still low at preleptotene stage.

In meiosis, RAD51 and DMC1 colocalization throughout the meiotic prophase reflects their cooperation at resected DSB ends [15–18,66]. In *Firrm* cKO and *Fignl1* cKO, RAD51 foci started to form earlier and their number was higher in early leptotene compared with DMC1 foci (Fig. 3b-c). We examined the colocalization of on-axis RAD51 and DMC1 foci from early leptotene (in *Firrm* cKO) and leptotene (in control) to mid-zygotene stage, in nuclei containing at least 10 foci for each protein (Fig.

4a-c; Extended Data Fig. 3a). As expected, on-axis RAD51 foci, the number of which was higher, colocalized less frequently with DMC1 foci in *Firrm* cKO than in control spermatocytes, especially at earlier stages (Fig. 4b). Conversely, more or similar percentages of on-axis DMC1 foci colocalized with on-axis RD51 foci in *Firrm* cKO and control spermatocytes at every stage, with a maximum in early leptotene (~70%). Off-axis foci in *Firrm* cKO displayed the same trend, with a very high percentage of DMC1 foci that colocalized with RAD51 foci at earlier stages (Extended Data Fig. 3b-e). Altogether, these observations indicate that in the absence of FIRRM, off-and on-axis RAD51 foci assemble independently of DMC1 foci in preleptotene and early prophase spermatocytes. Moreover, detectable DMC1 foci might form by joining pre-existing RAD51 foci, or by co-assembling *de novo* RAD51-DMC1 foci in *Firrm* cKO spermatocytes.

RAD51 and DMC1 form parallel linear structures along the synaptonemal complex in the absence of FIRRM

To refine the characterization of RAD51 and DMC1 distribution in *Firrm* cKO spermatocytes, we visualized RAD51, DMC1 and SYCP3 using super-resolution stimulated emission depletion (STED) microscopy (Fig. 4d-e). In leptotene and zygotene control spermatocytes, RAD51 and DMC1 formed partially overlapping co-foci along the unsynapsed axes and SC segments. RAD51 was more often closer to the chromosome axis than DMC1, as described previously [18,66]. In *Firrm* cKO spermatocytes, the patterns of RAD51 and DMC1 staining were more heterogeneous. A first type of RAD51-DMC1 co-foci was similar to control foci, but RAD51 signal tended to be more extended compared with DMC1 (Fig. 4d, compare control insets with the two upper panels of *Firrm* cKO insets). Second, some co-foci formed longer structures anchored to the chromosome axis, a pattern expected if they were extending along chromatin fibers (middle panels of the inset). Thus, the localization patterns of these two types of foci are compatible with RAD51/DMC1 filaments bound to chromatin fibers at DSB sites or/and dsDNA. In addition, at some sites, RAD51 and DMC1 followed the unsynapsed axes, often filling gaps with little or no SYCP3 signal between more heavily SYCP3-stained axis segments (bottom panels of the insets). Lastly, in *Firrm* cKO zygotene-like nuclei with some synapses, RAD51 and DMC1 formed two parallel lines separated by ~100 nm along SC segments, between the lateral elements (axes) visualized by ~210 nm apart SYCP3 signal (Fig. 4e-f). The intensity of these lines was irregular with interruptions, and interspersed with more intense foci. These observations suggest a highly aberrant patterning of RAD51 and DMC1 on meiotic chromatin and on meiotic chromosome axes in the absence of FIGNL1 and FIRRM activity.

Accumulation of RAD51 and DMC1 foci in *Firrm* cKO spermatocytes is meiotic DSB-independent

In *Firrm* cKO and *Fignl1* cKO spermatocytes, RAD51 and DMC1 displayed an unusual pattern that included an increased number of foci, many off-axis foci, and linear staining along chromosome axes. This was different from the expected discrete DSB repair foci on chromosome axes [16,62], raising the question of whether in these cKO models, RAD51 and DMC1 recruitment requires SPO11-generated DSBs. Thus, we generated *Spo11*$^{YF/YF}$ *Firrm* cKO double mutants in which SPO11 is catalytically dead [67]. The low early prophase γH2AX staining and the absence of RPA2 foci confirmed the absence of DSBs in these animals (Extended Data Fig. 4a-b). Strikingly, we detected large numbers of on-axis and off-axis RAD51 and DMC1 foci in *Firrm* cKO and in *Spo11*$^{YF/YF}$ *Firrm* cKO spermatocytes, and only background signal in *Spo11*$^{YF/YF}$ spermatocytes (as expected) (Fig. 5a). Overall, the pattern of RAD51 and DMC1 in *Firrm* cKO and *Spo11*$^{YF/YF}$ *Firrm* cKO were similar: a large number of on-axis foci detected from early prophase that persisted through zygotene, RAD51 foci formed during preleptotene stage, and both RAD51 and DMC1 off-axis foci progressively disappeared from leptotene to zygotene (Fig. 5b-c; Extended Data Fig. 5a-b). Moreover, RAD51 and DMC1 association, measured as the colocalization of on-axis foci, was similar in *Firrm* cKO and *Spo11*$^{YF/YF}$ *Firrm* cKO, indicating that their association is DNA damage-independent (Extended Data Fig. 5c-f).

DMC1 is recruited to DSB sites in the absence of the FIGNL1-FIRRM complex

The abundance of DSB-independent RAD51 and DMC1 foci raises the question of whether there is any recruitment at meiotic DSB sites in the absence of FIRRM or FIGNL1. Therefore, we determined the colocalization of on-axis DMC1 and RPA2 foci, used as a marker of a subset of the DSBs, in *Firrm* cKO and *Fignl1* cKO spermatocytes. The number of on-axis DMC1-RPA2 co-foci (corrected for random colocalization) in spermatocytes followed the kinetics of RPA2 foci in all genotypes (Extended Data Fig. 6a-d, compare with Fig. 2d). In *Firrm* cKO and *Fignl1* cKO spermatocytes, the percentage of on-axis RPA2 foci that colocalized with DMC1 was similar to control spermatocytes in leptotene and tended to be higher in mid-zygotene, possibly indicative of the accumulation of unrepaired HR intermediates (Fig. 6a; Extended Data Fig. 6e). The lower percentage of on-axis DMC1 foci that colocalized with RPA2 in cKO spermatocytes compared with control might be explained by the excess of DSB-independent DMC1 foci (Fig. 6b; Extended Data Fig. 6f). We obtained similar results also for on-axis RPA2-RAD51 co-foci in *Fignl1* cKO (Fig. 7e; Extended Data Fig. 8d). These findings suggest that the efficiency of RAD51 and DMC1 recruitment at sites of meiotic DSBs is not affected by FIRRM and FIGNL1 absence.

To assess directly DMC1 recruitment at SPO11-dependent DSB hotspots, we investigated the genome-wide distribution of DMC1-bound ssDNA by chromatin-immunoprecipitation (ChIP), followed by ssDNA enrichment (DMC1-Single Strand DNA Sequencing, SSDS) [68] in testes from 12-dpp control and *Firrm* cKO mice. In control mice, the regions enriched in DMC1-bound ssDNA are the ssDNA 3'overhangs that

result from DSB resection at meiotic DSB hotspots [69]. We detected 9,907 peaks in control and 7,397 peaks in *Firrm* cKO spermatocytes (Fig. 6c). Most of these peaks (6,614) were shared. Peaks called specifically in one genotype or the other were most likely shared weakly active hotspots, as inferred from their weak enrichment in both genotypes (Extended Data Fig. 7b). Most of the detected DMC1-SSDS peaks (9,297 out of 10,690) overlapped with previously identified meiotic SPO11-oligonucleotide DSB hotspots (SPO11-oligo hotspots, Extended Data Fig. 7a) [70]. Moreover, the DMC1-SSDS signal enrichment within peaks was highly correlated in control and *Firrm* cKO samples (Spearman's rho=0.92; Fig. 6d) with the exception of X chromosome hotspots, which were relatively less enriched in *Firrm* cKO than in control samples (Extended Data Fig. 7d). One possible explanation for this could be a genome-wide accumulation of HR intermediates in *Firrm* cKO that would erase the X chromosome-specific higher DMC1-SSDS enrichment due to delayed DSB repair [18,70,71]. Overall, this indicates that the recruitment of DMC1 on ssDNA at SPO11-dependent DSB hotspots was efficient, with relative hotspot intensities comparable to wild-type meiosis.

We then asked whether FIRRM depletion alters DMC1 extension on resected DSB ends at DSB hotspots. To characterize precisely the DMC1-SSDS signal distribution across DSB hotspots, we defined the center of overlapping SPO11-oligo hotspots as the center of our DMC1-SSDS peaks [70]. This improved significantly the quality of the average DMC1-SSDS signal profile, revealing a non-identical distribution in control and *Firrm* cKO (Extended Data Fig. 7b-c). Especially, we clearly observed a shoulder in the region of the curve surrounding the summit in control samples, as reported before, suggestive of a control mechanism ensuring a minimal DMC1 nucleoprotein filament length [18,70]. This shoulder was strongly reduced in *Firrm* cKO testes (Fig. 6e, Extended Data Fig. 7c). To improve the profile comparison, we normalized the overall signal intensity within common peaks in control and *Firrm* cKO samples and plotted the strand-specific average profiles of the normalized DMC1-SSDS signals (Fig. 6f). This confirmed that in *Firrm* cKO samples, DMC1-SSDS intensity started to progressively decrease immediately next to the narrow peaks that marked the 3' end of the ssDNA tails. This profile alteration was not dependent on the hotspot strength (Extended Data Fig. 7e). We also detected the same alteration at X chromosome hotspots, suggesting that this was not just a consequence of delayed DSB repair (Extended Data Fig. 7d). Moreover, the tail of DMC1 distribution extended a little further away. This wider distribution might be explained by more frequent longer DMC1 filaments, or by increased deposition of short DMC1 patches spread throughout the ssDNA tail. Altogether, the altered profile in *Firrm* cKO spermatocytes suggests that DMC1 recruitment at DSB sites remains efficient on a short DSB-proximal interval close to the 3' end of ssDNA tails independently of FIRRM, but that the mechanism controlling the DMC1 filament length requires FIRRM for full efficiency. One possible

scenario is that the FIGNL1-FIRRM complex controls the balance between DMC1 and RAD51 loading on ssDNA. Alternatively, we cannot exclude that the extent of DSB resection is altered.

Firrm cKO is epistatic to _Swsap1_ for controlling RAD51 and DMC1 loading

In mouse meiosis, the Shu complex component SWSAP1 is required for the assembly of normal numbers RAD51 and DMC1 foci, which are 2- to 3-fold fewer in *Swsap1*$^{-/-}$ than in wild-type leptotene-zygotene spermatocytes [40,41]. FIGNL1 depletion suppresses the defect of human SWSAP1-depleted cells in forming DNA damage-induced RAD51 foci, suggesting that SWSAP1antagonizes the anti-RAD51 activity of FIGNL1 [41]. We generated *Swsap1*$^{-/-}$ *Firrm* cKO and *Swsap1*$^{-/-}$ *Fignl1* cKO double mutant mice to determine if the defect in forming meiotic RAD51 and DMC1 foci in *Swsap1*$^{-/-}$ spermatocytes is similarly dependent on FIGNL1-FIRRM. We found that synapsis was defective and meiosis did not progress further than the zygotene-like stage with partial, partly non-homologous synapses in *Swsap1*$^{-/-}$ *Firrm* cKO and *Swsap1*$^{-/-}$ *Fignl1* cKO spermatocytes, like in *Firrm* cKO and *Fignl1* cKO single mutants. A small subset of nuclei progressed to pachynema, as observed for *Swsap1*$^{-/-}$ spermatocytes, most likely due to incomplete *Firrm* or *Fignl1* deletion. The double mutant spermatocytes accumulated RAD51 and DMC1, like *Firrm* cKO and *Fignl1* cKO spermatocytes (Fig. 7a-d, Extended Data Fig. 8a-c). However, because RAD51 and DMC1 accumulation in *Firrm* cKO and *Fignl1* cKO spermatocytes was essentially DSB-independent, this finding did not allow determining whether *Firrm* or *Fignl1* cKO relieves RAD51 and DMC1 recruitment at DSBs from SWSAP1 dependency. As a proxy for their localization at DSB sites, we measured RAD51 and DMC1 colocalization with RPA2 in *Swsap1*$^{-/-}$ *Fignl1* cKO spermatocytes. The fraction (Fig. 7e-f) of on-axis RPA2 foci colocalized with RAD51 and DMC1 was similar in control, in *Fignl1* cKO, and in *Swsap1*$^{-/-}$ *Fignl1* cKO spermatocytes (measured in one mouse per genotype). Reciprocally, equivalent numbers and fractions of on-axis RAD51 or DMC1 foci colocalized with RPA2 in *Fignl1* cKO and in *Swsap1*$^{-/-}$ *Fignl1* cKO spermatocytes (Extended Data Fig. 8d-e and 8f-g, respectively). Although the *Swsap1*$^{-/-}$ single mutant was missing in this experiment, the number of on-axis RAD51 or DMC1 foci colocalized with RPA2 exceeded the total number of RAD51 or DMC1 foci reported in leptotene-zygotene *Swsap1*$^{-/-}$ spermatocytes [40,41]. This suggests that the formation of detectable RAD51 and DMC1 foci at meiotic DSB sites might be independent of SWSAP1 in *Fignl1* cKO spermatocytes.

FIGNL1 perturbs the structure of RAD51/DMC1 nucleoprotein filaments and inhibits RAD51- and DMC1-mediated D-loop formation _in vitro_

To determine the HR step(s) in which FIGNL1-FIRRM might be involved, we examined *in vitro* the effect of adding FIGNL1 on the assembly and stability of RAD51 and DMC1 nucleofilaments, and on their subsequent strand invasion activity. We incubated preformed RAD51 or DMC1 filaments assembled

on a 400 nucleotide (nt) ssDNA or a 400 bp dsDNA with purified human FIGNL1ΔN (Extended Data Fig. 9a). FIGNL1ΔN did not promote RAD51 and DMC1 displacement from DNA (electrophoretic mobility shift assay in Fig. 8a-b, pre-formed nucleofilament), but induced the formation of a higher molecular weight complex, suggesting that FIGNL1ΔN binds to RAD51/DMC1-DNA filaments. When we mixed FIGNL1ΔN with RAD51 or DMC1 before addition to the DNA substrate, we observed a slight increase in the fraction of free dsDNA (but not ssDNA) that was not complexed with RAD51 or DMC1 (Figure 8a-c, no pre-formed nucleofilament). Whereas this increase was not significant, it might suggest that the presence of FIGNL1ΔN restricts RAD51 and DMC1 binding to DNA and the subsequent filament elongation. We then used transmission electron microscopy (TEM) to analyze the effect on RAD51 filament formation and architecture upon addition of FIGNL1ΔN at same time as RAD51 to a 400 nt ssDNA (Fig. 8d-e). Addition of FIGNL1ΔN induced the formation of super-complexes that contained several bridged or interwoven filaments. Simultaneously, we observed that individual RAD51 filaments not included in the super-complexes were significantly shorter than RAD51 filaments in controls (mean length of 135 versus 175 nm, respectively; Fig. 8f, Extended Data Fig. 9b). We also detected the formation of some very long filaments (more than 450 nm and up to 3-4 µm). Their length was not compatible with the length of the used DNA substrate, suggesting a DNA-independent polymerization in the presence of FIGNL1ΔN, which was confirmed by incubating RAD51 with FIGNL1ΔN without DNA (Extended Data Fig. 9b-d). Similarly, the mean length of RAD51 filaments assembled on a 400 bp dsDNA decreased from 194 nm in control to 137 nm in the presence of FIGNL1ΔN (Fig. 8f). The architecture of DMC1 filament assembled both on ssDNA and on dsDNA displayed qualitatively similar alteration (Extended Data Fig. 9c-d). Altogether, these results show that FIGNL1ΔN limits RAD51/DMC1 assembly on ssDNA and also dsDNA, and affect the filament architecture. We then tested whether these filaments could pair with homologous donor dsDNA (pUC19 plasmid) in a D-loop assay. Preformed RAD51, DMC1, and mixed RAD51-DMC1 filaments mediated the formation of 34, 27 and 22% of D-loop products, respectively. Addition of FIGNL1ΔN during filament assembly led to a decrease in the D-loop yield (Fig. 8g-h). When we titrated FIGNL1ΔN in the D-loop reaction, the yield decreased linearly and significantly (Fig. 8h). This showed that the contacting and pairing with homologous DNA of filaments assembled in the presence of FIGNL1ΔN might be affected. This indicates that by limiting the assembly of RAD51 and/or DMC1 on DNA, FIGNL1 could negatively regulate the next strand invasion step required for HR.

Discussion

The AAA-ATPase FIGL1 and its partner FIRRM were identified recently as negative regulators of meiotic COs in plants [44,47–49], and FIGNL1 as a negative regulator of RAD51 in human cells [41,43], but their role in mammalian meiosis remained unknown. Here, by characterizing male germ line-specific *Fignl1* and *Firrm* cKO mouse models, we uncovered two roles of the FIGNL1-FIRRM complex in male meiosis. First, FIGNL1 and FIRRM are required for meiotic DSB repair and for homologous chromosome synapsis during meiotic prophase I, and thus are essential for male mouse meiosis. Second, the FIGNL1-FIRRM complex prevents DNA damage-independent accumulation of RAD51 and DMC1 on chromatin and chromosome axes in spermatocyte nuclei during premeiotic replication and meiotic prophase I. Shinohara's group reached similar conclusions by characterizing the *Fignl1* cKO mouse in a study reported in the accompanying article.

Our data show that FIGNL1 and FIRRM act as negative regulators of RAD51 and DMC1 during meiotic recombination, a function evolutionarily conserved from plants to mammals. However, the role of FIGNL1-FIRRM is much more crucial in mouse spermatogenesis than in *A. thaliana* and rice meiosis where homologous chromosome synapsis and formation of ZMM-dependent type I COs are almost normal in FIGNL1 and FIRRM mutants [44,47–50]. Plants and mammals show differences in their requirement of specific HR pathways for meiotic DSB repair, homologous chromosome synapsis and progression through meiotic cell cycle. These processes require DMC1, MSH4 and MSH5 in the mouse [12–14,60,72]. Conversely, in *A. thaliana* and rice, meiotic DSBs are repaired by RAD51-dependent intersister HR in *dmc1* mutants, homologous chromosome synapsis does not depend on MSH4-MSH5, and *dmc1*, *msh4* and *msh5* mutant cells progress through meiotic prophase (reviewed in [73]). These differences might explain why FIGNL1 or FIRRM deficiency might lead to a stronger phenotype in mice than in plants. However, mouse *Fignl1* cKO and *Firrm* cKO spermatocytes also displayed defects not seen in plants, especially a massive, DNA damage-independent RAD51 and DMC1 accumulation and defects in MSH4 focus formation. This suggests that the FIGNL1-FIRRM complex has additional functions in the mouse within the shared framework of RAD51 and DMC1 negative regulation.

We found that in *Fignl1* cKO and *Firrm* cKO spermatocytes, MSH4 focus formation and meiotic DSB repair were impaired, RAD51 and DMC1 foci accumulated at unrepaired DSB sites, and homologous synapsis was defective. These defects have been described in mutants in which strand invasion is impaired (e.g. *Dmc1*$^{-/-}$ mice that accumulate only RAD51, *Hop2*$^{-/-}$, *Mnd1*$^{-/-}$ mice)[5,6,60,72,74–76] and in mutants in which strand invasion might be preserved but the HR intermediates are not efficiently stabilized (e.g. *Hrob*$^{-/-}$, *Mcm8*$^{-/-}$, *Mcmd2*$^{-/-}$, *Msh4*$^{-/-}$, *Msh5*$^{-/-}$ mice) [12–14,77–80]. By altering the stability or architecture of the nucleoprotein filament formed by RAD51/DMC1 on ssDNA and/or dsDNA, the FIGNL1-FIRRM complex might play a role before or after strand invasion. In the case of a post-strand

invasion role, this complex might favor RAD51/DMC1 dissociation from dsDNA in the D-loop, a step required for initiating DNA synthesis to extend the invading strand. In *S. cerevisiae*, the motor protein Rad54 and its paralog Rdh54 are involved in removing RAD51/DMC1 from dsDNA following D-loop formation [28,32]. In the mouse, the meiotic function of RAD54 and its paralog RAD54B is not crucial because *Rad54 Rad54b* double mutant mice are fertile, although they display persistent RAD51 foci during meiotic prophase [33,34]. Thus, additional factors can disassemble RAD51 and DMC1 from the D-loop. The FIGNL1-FIRRM complex might promote RAD51/DMC1 dissociation from dsDNA after strand invasion by destabilizing the filament. In our *in vitro* assay, human FIGNL1ΔN could not dissociate preformed RAD51/DMC1 filaments; however, the full length FIGNL1-FIRRM complex might possess a stronger activity sufficient to dissociate RAD51/DMC1 efficiently. Alternatively, FIGNL1-FIRRM complex -dependent RAD51/DMC1 filament alteration might render it sensitive to dismantling by other factors. In addition to normal HR intermediate processing, the FIGNL1-FIRRM complex might also dissociate unproductive or potentially toxic post-synaptic RAD51/DMC1 filaments, such as multiple strand invasion or invasion on non-allelic repeated sequences [81,82].

In *Firrm* cKO spermatocytes, the average DMC1-SSDS signal profile at meiotic DSB hotspots was altered in a way that suggests that FIRRM may be involved in regulating the length of DMC1-ssDNA filaments. In wild-type mouse spermatocytes, the profile of DMC1-SSDS coverage at DSB hotspots and super-resolution microscopy observations indicate that DMC1 typically occupies the DSB-proximal two-third of the DSB 3' ssDNA end, and RAD51 the DSB-distal third of the same DSB 3' ssDNA end [5,6,16,18,66,70]. DMC1 and RAD51 segregation along ssDNA tails might result from the formation of a stable DMC1 filament or/and from the prevention of RAD51 loading on the 3' region of the ssDNA tail. In the context of inhibited RAD51 catalytic activity during meiosis, interhomolog recombination relies on DMC1 catalytic activity [18–20]. Therefore, defects in regulating the length or the continuity of the active DMC1 filament may affect the efficiency of interhomolog search [82], the formation of a D-loop that can be stabilized by MSH4-MSH5, and homologous chromosome synapsis. Several non-exclusive hypotheses can be proposed to explain how the FIGNL1-FIRRM complex regulates the DMC1 filament on DSB 3' ssDNA tails. First, RAD51 nuclear fraction was increased in *Fignl1* cKO and *Firrm* cKO testes (Fig. 1a), suggesting that RAD51 might outcompete DMC1 on ssDNA tails in these mutants. It has been suggested that BRCA2 promotes RAD51 nuclear import by limiting the formation of cytoplasmic RAD51 polymers which cannot be mobilized [83]. We also found that RAD51 forms DNA-independent filaments in the presence of purified human FIGNL1ΔN (Extended Data Fig. 9c-d). Therefore, the balance between FIGNL1-FIRRM and BRCA2 might control the level of cytoplasmic RAD51 polymerization, contributing to fine-tune RAD51 nuclear level (Fig. 8i, (i)). We could also suggest that the FIGNL1-FIRRM complex has a more direct role in controlling the formation of RAD51 and DMC1 filaments at DSB

ssDNA overhangs, based on a previously proposed model (Fig. 8i, (iii)) [9]. *In vitro*, RAD51 nucleates randomly on ssDNA tracts, whereas DMC1 prefers to seed at a ds/ssDNA junctions or on a RAD51 patch (by analogy with *S. cerevisiae*), and polymerizes specifically in the 5' to 3' direction [84]. We hypothesize that the FIGNL1-FIRRM complex may disassemble nascent RAD51-ssDNA patches that would otherwise hamper DMC1 filament extension toward the 3' end of ssDNA tails. According to this hypothesis, the formation of dispersed RAD51 patches in *Firrm* cKO spermatocytes would impede the polymerization of extended DMC1 filaments and consequently reduce DMC1 occupancy in the 3' region of ssDNA tails. Specific accessory factors (e.g. the SWSAP1-SWS1-SPIDR complex) might protect RAD51 from the FIGNL1-FIRRM complex on the DSB-distal part of ssDNA tails. Indeed, the SWSAP1-SWS1-SPIDR complex is required to form normal numbers of RAD51/DMC1 foci during meiosis [36,40–42]. Moreover, FIGNL1 interacts with SWSAP1 and SPIDR [37,41,43], and SWSAP1 protects RAD51 filaments from FIGNL1 *in vivo* and *in vitro* [41]. Interestingly, it was recently reported that in human cells, SWSAP1-SWS1 interact with the cohesin regulatory protein PDS5B, which localizes to chromosome axes during meiotic prophase [37,85]. As generally RAD51 localizes closer to the chromosome axis than DMC1 in mouse meiotic prophase [18,66], this interaction, if present in meiotic prophase, might provide an anchor that favors preferential RAD51 protection on the DSB-distal part of DSB ssDNA tails. Alternatively, we cannot exclude that DMC1-SSDS profile alterations are due to accumulating HR intermediates with a biased DMC1-ssDNA distribution. For example, longer DMC1 filaments might be more frequently engaged in strand invasion, therefore bound on dsDNA and undetectable by ChIP-SSDS, compared with shorter filaments.

In *Fignl1* cKO and *Firrm* cKO spermatocytes, we observed meiotic DSB-independent accumulation of RAD51 foci on chromatin during premeiotic replication that persisted and was accompanied by DMC1 accumulation during meiotic prophase. DNA damage-independent RAD51 foci accumulate in human cells upon RAD51 overexpression [29], thus higher RAD51 nuclear concentration in the absence of FIRRM or FIGNL1 might contribute to favor DNA damage-independent RAD51 and DMC1 binding on intact chromatin (Fig. 8i, (i)). In addition, RAD51 and DMC1 DNA damage-independent accumulation is observed in budding yeast and human cells after depletion of RAD54 family DNA translocases [29–31]. By analogy, the FIGNL1-FIRRM complex might prevent the stabilization of normally transient nascent RAD51-dsDNA filaments at replication forks (Fig. 8i, (ii)). This hypothesis is consistent with our finding that purified human FIGNL1ΔN might reduce RAD51 and DMC1 association with dsDNA *in vitro* (Fig. 8b-c), and with a recent study in human cells showing FIGNL1-FIRRM association with ongoing replication forks in unchallenging conditions [86].

514 The linear RAD51/DMC1 staining detected between SYCP3 synapsed axes suggests that RAD51/DMC1
515 can associate stably with chromosome axis components, in either a DNA-dependent or DNA-
516 independent manner, in the absence of the FIGNL1-FIRRM complex. DSB-independent RAD51 (but not
517 DMC1) staining along unsynapsed chromosome axes has been previously described in late prophase
518 mouse oocytes [67,87,88]; however, these structures associating RAD51 and DMC1 along synapsed axes in
519 *Fignl1* cKO and *Firrm* cKO spermatocytes are unusual. RAD51 interacts with several components of
520 meiotic chromosomes, including the axis component SYCP3 [15], the SC central element component
521 SYCE2 [89,90] and the cohesion regulator PDS5A/B [91,92] that interacts also with SWSAP1-SWS1 [37].
522 Interestingly, it has been observed by super-resolution microscopy that several cohesin subunits and
523 HORMAD1/2 coat the outside of SYCP3 axis cores [66,93], a localization resembling that of RAD51/DMC1
524 staining between synapsed SYCP3-positive axes. RAD51/DMC1 interactions with components of
525 meiotic chromosome axes might facilitate the accurate HR repair of meiotic DSBs (and incidental DNA
526 damages). In this context, a function of the FIGNL1-FIRRM complex might be to prevent the
527 stabilization, of these interactions, other than at DNA damage sites.
528
529 Meiotic cells must face the challenge of repairing hundreds of programmed DSBs through several HR
530 pathways, while restricting inappropriate repair that may involve similar HR intermediates. In this
531 study, we started deciphering the functions of the conserved FIGNL1-FIRRM complex in mouse
532 meiosis. We showed that the RAD51/DMC1 filament destabilizing activity of FIGNL1 and FIRRM is
533 implicated in regulating meiotic recombination and restricting inappropriate formation of stable
534 RAD51/DMC1 filaments. Interestingly, although FIGNL1 alters RAD51 and DMC1 filament similarly *in*
535 *vitro*, it is not clear whether FIGNL1 or FIRRM absence affects DMC1 directly or indirectly through
536 RAD51. The elucidation of the several possible functions of the FIGNL1- FIRRM complex during mouse
537 meiosis will need more *in vitro* and *in vivo* analyses of their functional interactions with other RAD51
538 and DMC1 regulators.
539
540
541 **Methods**
542 **Mice**
543 All mice used in the study were in the C57BL/6J background. *Firrm*$^{fl/+}$ mice (allele
544 *BC055324*$^{tm1c(EUCOMM)Hmgu}$, MGI:5692863) were obtained from the International Knockout Mouse
545 Consortium (IKMC). *Fignl1*$^{fl/+}$ mice (allele *Fignl1*$^{tm1c(EUCOMM)Hmgu}$) were generated by Phenomin-Institut
546 Clinique de la Souris (ICS) using the plasmid containing the *Fignl1*$^{tm1a(EUCOMM)Hmgu}$ allele (MGI:5287847)
547 obtained from Helmholtz Zentrum München GmbH. *Firrm*$^{fl/fl}$ mice were mated with mice that express
548 Cre under the control of the CMV promoter (C57BL/6 Tg(CMV-cre)1Cgn) [94] to generate *Firrm*-deleted

heterozygous mice (*Firrm*$^{+/-}$). *Firrm*$^{+/-}$ mice were mated with Tg(Stra8-icre)1Reb/J (*Stra8-Cre*^{Tg}) mice [52] to generate *Firrm*$^{+/-}$*;Stra8-Cre*^{Tg} mice. By crossing *Firrm*$^{fl/fl}$ mice with *Firrm*$^{+/-}$*;Stra8-Cre*^{Tg} mice, *Firrm*$^{fl/-}$*;Stra8-Cre*^{Tg} (*Firrm* cKO) and *Firrm*$^{fl/+}$, *Firrm*$^{fl/+}$ *Stra8-Cre*^{Tg} or *Firrm*$^{fl/-}$ (*Firrm* control) mice were obtained. *Fignl1*$^{fl/-}$*;Stra8-Cre*^{Tg} (*Fignl1* cKO) mice were generated using the same strategy as for *Firrm* cKO mice. The *Spo11*$^{YF/YF}$ [67] and *Swsap1*$^{-/-}$ [95] mouse lines were described previously. Primers used for genotyping are listed in Supplementary Table 1. All animal experiments were carried out according to the CNRS guidelines.

Histology

Mouse testes were fixed in Bouin's solution for periodic acid-Schiff (PAS) staining at room temperature, overnight. Testes were then embedded in paraffin and 3µm-thick slices were cut. PAS-stained sections were scanned using the automated tissue slide-scanning tool of a Hamamatsu NanoZoomer Digital Pathology system.

Spermatocyte chromosome spreads

Spermatocyte spreads were prepared with the dry down technique [96]. Briefly, a suspension of testis cells was prepared in PBS, and then incubated in a hypotonic solution for 8 min at room temperature. Cells were centrifuged, resuspended in 66 mM sucrose solution and spread on slides or coverslips (1.5H, high precision) with 1% paraformaldehyde, 0.05% Triton X-100. Slides/coverslips were dried in a humid chamber for 1-2 h, washed in 0.24% Photoflo200 (Kodak), air-dried, and used for immunostaining or stored at -80°C.

Immunofluorescence staining

Immunostaining was done as described [97]. After incubation with a milk-based blocking buffer (5% milk, 5% donkey serum in PBS), spermatocyte spreads were incubated with primary antibodies at room temperature overnight, followed by secondary antibodies (37 °C for 1 h). The used antibodies are listed in Supplementary Table 2. Nuclei were stained with 4'−6-diamidino-2-phenylindole (DAPI, 2 µg/ml) in the final washing step.

For immunostaining with the anti-DMC1 antibody, a specific blocking buffer (0.5% BSA, 0.5% powder milk, 0.5% donkey serum in PBS) was used prior to incubation with the primary antibody that was performed in 10% BSA in PBS. Immunostaining of spermatocyte spreads on coverslips for STED microscopy was done with specific secondary antibodies (Supplementary Table 2), and DAPI was omitted.

Widefield fluorescent imaging

Widefield images were acquired using one of the following microscopes: Zeiss Axioimager Apotome with 100X Plan Apochromat 1.46 oil DIC objective and 1 ANDOR sCMOS ZYLA 4.2 MP monochrome camera (2048 x 2048 pixels, 6.5µm pixel size) or Zeiss Axioimager 100X Plan Apochromat 1.4 NA oil objective and 1 Zeiss CCD Axiocam Mrm 1.4 MP monochrome camera (1388 x 1040 pixels, 6.45µm pixel size).

Stimulated emission depletion (STED) super-resolution imaging

Super-resolution images were acquired using a STED microscope (Abberior Instruments, Germany) equipped with a PlanSuperApo 100x/1.40 oil immersion objective (Olympus, Japan). For 3-color STED imaging, immunolabeling was performed using one of the following combinations of secondary antibodies: STAR 460L, STAR ORANGE, STAR RED or STAR GREEN, STAR ORANGE, STAR RED (Supplementary Table 2). STAR 460L and STAR 488 were excited at 485nm, STAR ORANGE at 561nm, and STAR RED at 640nm. Excitation was done with a dwell time of 10µs. STED was performed at 595 nm for STAR 488 and at 775nm for all other dyes. Images were collected in line accumulation mode with detection set at 571-625nm for STAR 460L and STAR ORANGE, 500-580nm for STAR GREEN, and 650-750nm for STAR RED.

Image analysis

For quantification and colocalization analyses, images were deconvolved using Huygens Professional version 22.10 (Scientific Volume Imaging).

All image analyses were performed using Fiji/ImageJ 1.53t [98].

Single nuclei were cropped manually or using an automatic DAPI signal threshold. Nuclei were sorted into meiotic prophase substages following the criteria described below.

Foci were detected using the Find Maxima function. On-axis and off-axis foci were distinguished on the basis of their localization within (or outside) a binary mask. This ROI was drawn using an automatic SYCP3 axis protein staining threshold (SYCP1 staining was used for MSH4 and TEX11 foci). Because there was no SYCP3 staining-defined axis structure at preleptotene stage, all foci were considered as off-axis foci at this stage.

For two-color focus colocalization, the distance of a given channel focus to the closest second color focus was calculated. Foci were considered as colocalized when this distance was below the minimum resolution distance (0.3µm for widefield images), as in [99]. The level of random colocalization of foci in channel A (foci A) with foci in channel B (foci B) in any given nucleus was estimated by simulating the random localization of the actual number of foci A, and by determining the number of random foci A colocalized with actual foci B. The mean number of colocalizations from 100 simulations was taken as

the number of foci A colocalized with foci B by chance in the nucleus (n_{random}, "random" on figures), and this was repeated for every nucleus. Reciprocally, the level of random colocalization of foci B with foci A resulted from random simulations of foci B localizations.

In every nucleus, the number of colocalized foci A was corrected for random colocalization by considering that (1) the observed number of colocalized foci A (n_{obs}) is composed of one subset of biologically meaningful colocalized foci ("truly" colocalized foci A, n_{col}) and one subset of foci A colocalized by chance; (2) the ratio n_{random} /n_T (where n_{random} is estimated as described above and n_T is the total number of foci A in the nucleus) estimates the frequency of foci A colocalizing by chance among the population of foci A not "truly" colocalized, thus the number of foci A colocalized by chance is ($n_T - n_{col}$) * n_{random} /n_T , by excluding the truly colocalized foci A from random colocalization.(3) Finally, the estimated number of colocalized foci corrected for random colocalization ($n_{col,}$) was obtained from the formula $n_{col}=(n_{obs}-n_{random})/(n_T-n_{random})$, where n_{tot} was the total number of foci counted, n_{obs} the observed number of colocalized foci and n_{random} the mean number of colocalization from 100 simulations as described above. The percentage of corrected colocalization estimate was the ratio of the corrected number of colocalized foci n_{col} over the total number of foci in the same nucleus, n_{col} / n_T.

For γH2AX quantification, nuclei were cropped manually and the integrated intensity of the γH2AX channel in the cropped region was measured.

Prophase spermatocytes were staged using the following criteria, based on SYCP3 staining. Preleptotene nuclei had patchy weak SYCP3 signal throughout the nucleus. Early leptotene nuclei had focus-like well-defined very short stretches of SYCP3 staining. Leptotene nuclei had short stretches of SYCP3 fragments. Early zygotene nuclei had longer SYCP3 stretches as the chromosome axes continued to elongate. Mid-zygotene nuclei had very long or full SYCP3 axes, but no or relatively few synapses marked by thicker SYCP3 stretches. Late zygotene had full SYCP3 axes with extensive synapsis marked by thicker SCP3 signal.

DMC1 chromatin immuno-precipitation, followed by single-strand DNA sequencing (DMC1-SSDS)

DMC1 ChIP-SSDS and library preparation were performed as described in [100] using a goat anti-DMC1 antibody (0.5 mg/ml; Santa Cruz, reference C-20). Ten testes from 12 dpp *Firrm*$^{fl/+}$*;Stra8-Cre*^{Tg} (control) and from *Firrm*$^{fl/+}$*;Stra8-Cre*^{Tg} (*Firrm* cKO) mice were used in each biological replicate. Sequencing was performed on a NovaSeq 6000 PE150 platform in paired end mode (2x150bp).

Detection of DMC1 ChIP-SSDS peaks

Raw reads were processed using the SSDS-DMC1 Nextflow pipeline (Auffret et al., MiMB Germ Cells Development, in prep.), available on github (https://github.com/jajclement/ssdsnextflowpipeline , see details of the pipeline development on the README page). Briefly, the main steps of the pipeline included raw read quality control and trimming (removal of adapter sequences, low-quality reads and extra bases) and mapping to the UCSC mouse genome assembly build GRCm38/mm10. Single stranded derived fragments were then identified from mapped reads using a previously published method [68,101], and peaks were detected in Type-1 fragments (high confidence ssDNA). To control reproducibility and assess replicate consistency, the Irreproducible Discovery Rate (IDR) method [102] was used, following the ENCODE procedure (https://github.com/ENCODE-DCC/chip-seq-pipeline2). The "regionPeak" peak type parameter and default p-value thresholds were used. Briefly, this method performs relaxed peak calling for each of the two replicates (truerep), the pooled dataset (poolrep), and pseudo-replicates that are artificially generated by randomly sampling half of the reads twice, for each replicate and the pooled dataset. Both control and *Firrm* cKO datasets passed the IDR statistics criteria for the two scores (well below 2). By default, the pipeline gave the poolrep as primary output, but for this study the truerep peak sets were considered. Lastly, peak centering and strength calculation were computed using a previously published method [68].

The list of SPO11-oligo hotspots from B6 mice and the coordinates (genome build GRCm38/mm10) of their center were from [70].

The overlaps between intervals was determined with bedtools [103] Intersect on the Galaxy France web interface. For determining overlaps between control and *Firrm* cKO peaks, a minimum overlap of 10%, and reciprocally, was required. The overlap between DMC1-SSDS peaks and the center of SPO11-oligo hotspots [70] was considered positive if at least 1 bp of the DMC1-hotspot contained the coordinate of the center of one SPO11-oligo hotspot.

Heatmaps and average plot profiles were generated with deeptools (computeMatrix, plotHeatmap and PlotProfile) on Galaxy France server.

Preparation of mouse testis protein extracts and western blotting

Cytoplasmic and nuclear extracts were prepared from 12 dpp control, *Firrm* cKO and *Fignl1* cKO mice. Testes were homogenized in hypotonic buffer (10 mM Hepes, pH 7.4, 320 mM sucrose, 0.2 mM PMSF, 1x Complete protease inhibitor cocktail, EDTA-free (Roche), 0.07% beta-mercaptoethanol) in a Dounce homogenizer. After centrifugation (1,000xg at 4°C for 10 min), the supernatant was collected and used as cytoplasmic fraction. The pellet was resuspended in half nuclear packed volume of low salt buffer (20mM Tris-HCl pH7.3, 12.5% glycerol, 1.5mM $MgCl_2$, 0.2mM EDTA, 20mM KCl, 1x Complete protease inhibitor cocktail, EDTA-free (Roche), 0.07% beta-mercaptoethanol). Then half nuclear packed volume of high salt buffer (same, but 1.2M KCl) was added drop by drop, incubated at 4°C for 30min with

agitation and centrifuged (14,000xg at 4°C for 30 min). The supernatant was collected as nuclear fraction. Cytoplasmic and nuclear fractions were analyzed by western blotting with rabbit anti-FIGNL1 (1/500, Proteintech, 17604-1-AP), rabbit anti-FIRRM (1/500, Abcam, ab121774), rabbit anti-beta tubulin (1/3000, Abcam, ab6046) and guinea pig anti-SYCP3 (1/3,000 [97]) antibodies. HRP-conjugated secondary antibodies were anti-rabbit IgG-HRP (1:5,000; Cell Signaling Technology) and donkey anti-guinea pig IgG-HRP (1/10,000; Jackson Immuno Research, 706-035-148).

Protein purification. Human RAD51 was purified by the CiGEX Platform (CEA, Fontenay-aux-Roses) as follows. His-SUMO-RAD51 was expressed in the *E. coli* strain BRL (DE3) pLys. All protein purification steps were carried out at 4°C. Cells from a 3-liter culture that was induced with 0.5 mM isopropyl-1-thio-ß-D-galactopyranoside (IPTG) at 20°C overnight were resuspended in 1x PBS, 350 mM NaCl, 20 mM imidazole, 10% glycerol, 0.5 mg/ml lysozyme, Compete Protease Inhibitor (Roche), 1 mM 4-(2-aminoethyl)benzenesulfonyl fluoride (AEBSF). Cells were lysed by sonication and the insoluble material was removed by centrifugation at 150,000 x g for 1h. The supernatant was incubated with 5 ml of Ni-NTA resin (Qiagen) for 2h. The mixture was poured into an Econo-Column Chromatography Column (BIO-RAD) and beads were washed first with 80 ml W1 buffer (20 mM Tris HCl pH 8, 500 mM NaCl, 20 mM imidazole, 10% glycerol, 0.5% NP40), followed by 80 ml of W2 buffer (20mM Tris HCl pH 8, 100mM NaCl, 20mM imidazole, 10% glycerol, 1 mM DTT). Then, His-SUMO-RAD51 bound to the beads was resuspended in 8ml of W2 buffer and incubated with SUMO protease at a 1/80 ratio (w/w) for 16 h. RAD51 without the His-SUMO tag was then recovered into the flow thru and directly loaded onto a HiTrap heparin column (GE Healthcare). The column was washed with W2 buffer and then a 0.1-1M NaCl gradient was applied. Fractions containing purified RAD51 were concentrated and dialyzed against storage buffer (20mM Tris HCl pH 8, 50mM KCl, 0.5 mM EDTA, 10% glycerol, 1 mM DTT, 0.5 mM AEBSF) and stored at -80°C. Human RPA was purified by the CiGEX Platform (CEA, Fontenay-aux-Roses) as previously described [104].

For human FIGNL1 purification, *FIGNL1ΔN* without the region encoding the N-terminal 284 aa was inserted into the pET15 vector (Novagene), and the protein was overexpressed in *E. coli* BL21(DE3) cells upon addition of 0.2mM IPTG at 37°C for 3h. Cell pellets were resuspended in buffer A (50mM Tris-HCl pH7.4, 500 mM NaCl, 5% glycerol, 5mM $MgCl_2$, 5 mM β-mercaptoethanol, 1 mM PMSF, 0.1% NP40, 20 mM imidazole, cOmplete Protease Inhibitor Cocktail), disrupted by French press (6 bar) and cleared by centrifugation following incubation with the benzonase nuclease (Sigma) at 4°C for 30 min. The supernatant was loaded on a 1 ml HisTrap Fast-Flow column (GE healthcare) and equilibrated with buffer A on an ÄKTA pure system. After a washing step, proteins were eluted with buffer A supplemented with 300 mM imidazole. FIGNL1ΔN was further purified by size exclusion chromatography using a HiLoad 16/600 Superdex 200 column (GE Healthcare) in buffer B (50mM Tris-

HCl pH7.4, 200 mM NaCl, 10% glycerol, 5mM $MgCl_2$, 5 mM β-mercaptoethanol). The peak fractions were concentrated with Amicon Ultra 30K (Millipore) and stored at -80°C.

RAD51 and DMC1 filament electromobility shift assay (EMSA). RAD51 and DMC1 filaments were formed by incubating 3 μM (nucleotide concentration) of 400 nt ssDNA or dsDNA labeled with Cy5 with 1 μM RAD51 (1 protein per 3 nt) or 1.5 μM DMC1 (>1 protein per 3 nt to obtain fully covered DNA) in a buffer containing 10 mM Tris-HCl pH7.5, 50 mM NaCl, 2 mM $MgCl_2$, 2 mM $CaCl_2$, 2 mM ATP, and 1 mM DTT at 37°C for 20 min. Then, 1.6 μM of FIGLN1ΔN was added to the reaction to test their effects on filament assembly and architecture (pre-formed filament). Alternatively, RAD51 or DMC1 was added concomitantly with FIGLN1ΔN to the reaction (no pre-formed filament). Protein-DNA complexes were fixed in 0.01% glutaraldehyde at room temperature for 5 min. Then, the reaction products were analyzed using 1% agarose gel in 0.5x Tris acetate/EDTA at 4 ˚C. Images were acquired using a Typhoon imager (GE Healthcare Life Science).

Tramsmission electron microscopy (TEM) analysis of RAD51 and DMC1 filaments. RAD51 and DMC1 filaments were formed by incubating 7.5 μM (nucleotide concentration) of 400 nt long ssDNA and dsDNA with 2.5 μM RAD51 (1 protein per 3 nt) or 3.5 μM DMC1 in a buffer containing 10 mM Tris-HCl pH7.5, 50 mM NaCl, 2 mM $MgCl_2$, 2 mM $CaCl_2$, 2 mM ATP and 1 mM DTT at 37°C for 20 min. Then, 1.6 μM of FIGLN1ΔN was added to the reaction at the same time as RAD51/DMC1. For filament length analysis, positive staining combined with a TEM dark-field imaging mode were used: 1 μL of the reaction was quickly diluted 20 times in a buffer containing 10 mM Tris-HCl pH 7.5, 50 mM NaCl, 2 mM $MgCl_2$, 2 mM $Cacl_2$. During one minute, a 5 μL drop of the dilution was deposited on a 600-mesh copper grid previously covered with a thin carbon film and pre-activated by glow-discharge in the presence of amylamine (Sigma-Aldrich, France) [105,106]. Grids were rinsed and positively stained with aqueous 2 % (w/v) uranyl acetate, dried carefully with a filter paper. To better observe FIGLN1ΔN effect on the filament architecture, samples were also spread using negative staining and observed in bright-field mode. For this, a drop of the reaction was directly deposited on a carboned copper grid pre-activated with glow discharge (plasma).

TEM grids were observed in the annular dark-field mode in zero-loss filtered imaging or in canonical bright-field imaging using a Zeiss 902 transmission electron microscope. Images were captured at a magnification of 85,000× with a Veleta CCD camera and analyzed with the iTEM software (both Olympus Soft Imaging Solution). For quantification, the filament length was measured in at least two independent experiments with a total of at least 75 molecules measured.

D-loop *in vitro* assay. RAD51 and DMC1 filaments were formed in the same conditions as for the EMSA analysis. The same incubation conditions and buffer were used to assemble mixed RAD51/DMC1 filaments by incubating 3 μM (nucleotide concentration) of 400 nt ssDNA substrates with 1.25 μM RAD51 plus 0.75 μM DMC1. In the second step, 15 nM in molecules of homologous dsDNA donor (pUC19 plasmid purified on MiniQ ion exchange chromatography column) was introduced in the reaction and in case of DMC1 filaments, 4 mM more $CaCl_2$ was added, and then the mixture was incubated at 37°C for 30 min. The reaction was stopped with 0.5 mg/mL proteinase K, 1% SDS, 12.5 mM EDTA at 37°C for 30 min and separated on 1% TAE agarose gels (80 V, for 30 min).

Statistical analysis and reproducibility

The statistical analyses of cytological observations were done with GraphPad Prism 9. A contingency chi-square test was used to compare stage distributions. The nonparametric Mann-Whitney test was used to compare focus counts, colocalized focus counts and fractions, and γH2AX intensity among genotypes. The nonparametric Wilcoxon signed-ranks test was used to compare true colocalization versus random colocalization of foci. All tests, sample size, and p values (n.s., not significant, *P < 0.05, **P < 0.01, ***P < 0.001, ****P < 0.0001) are provided in the corresponding legends and/or figures. If not otherwise stated, at least two animals/genotype were analyzed and similar results were obtained.

Data availability

The DMC1-SSDS raw and processed data for this study have been deposited in the European Nucleotide Archive (ENA) at EMBL-EBI and are available through the project identifier PRJEB62127.

Acknowledgements

We would like to thank Masaru Ito and Akira Shinohara for sharing unpublished results, Maria Jasin for *Swsap1* mice, Qinghua Shi for the guinea-pig anti-DMC1 antibody. We thank Raphaël Mercier for encouraging the project, and Thomas Robert for critical reading of the manuscript. We thank the following Montpellier Biocampus facilities for their service: Anne Sutter and the animal facility (RAM) for animal care, Manon Leportier for managing our mouse strains, the Réseau d'Histologie Expérimentale de Montpellier (RHEM) for histology. We acknowledge the support of Marie-Pierre Blanchard for help with STED microscopy and the imaging facility MRI, member of the national infrastructure France-BioImaging infrastructure supported by the French National Research Agency (ANR-10-INBS-04, "Investments for the future"). We are grateful to Xavier Veaute from the CiGEX Platform (CEA, Fontenay-aux-Roses), and to the https://www.france-bioinformatique.fr/ and the https://www.france-bioinformatique.fr/fr/cluster for providing computing resources on Galaxy France.

This work was supported by the Agence Nationale de la Recherche ANR FIRE (ANR-17-426 CE12-0015) to FB, PD, JBC and RK; by the Ligue contre le Cancer (Comité départemental de l'Hérault and Comité départemental du Gard) to FB; by the Ligue contre le Cancer (MB/CB/070-22) to RK. AZ was funded by ANR FIRE (ANR-17-426 CE12-0015) and a PhD fellowship FDT202106012805 from the Fondation pour la Recherche Médicale (FRM).

Author contributions

AZ, PD, RK and FB conceived and designed the experiments. AZ performed most mouse experiments, SB and FB performed some mouse experiments. AZ and FB interpreted and analyzed mouse data with input from BdM. PD, VR, RK performed, analyzed and interpreted biochemical experiments with contribution from JBC. JC developed the method for image analysis. PA and JAJC developed the bioinformatic pipeline for analyzing SSDS data. JAJC and FB performed bioinformatic analysis of SSDS data. AZ, PD, RK and FB wrote the manuscript with input from all authors.

Competing interests

The authors declare no competing interests.

References

1. Gerton, J. L. & Hawley, R. S. Homologous chromosome interactions in meiosis: diversity amidst conservation. *Nat Rev Genet* **6**, 477–487 (2005).
2. Hunter, N. Meiotic Recombination: The Essence of Heredity. *Cold Spring Harb Perspect Biol* **7**, a016618 (2015).
3. Baudat, F., Imai, Y. & de Massy, B. Meiotic recombination in mammals: localization and regulation. *Nat Rev Genet* **14**, 794–806 (2013).
4. Robert, T., Vrielynck, N., Mézard, C., de Massy, B. & Grelon, M. A new light on the meiotic DSB catalytic complex. *Seminars in Cell & Developmental Biology* **54**, 165–176 (2016).
5. Paiano, J. *et al.* ATM and PRDM9 regulate SPO11-bound recombination intermediates during meiosis. *Nature Communications* **11**, (2020).
6. Yamada, S. *et al.* Molecular structures and mechanisms of DNA break processing in mouse meiosis. *Genes & development* **34**, 806–818 (2020).

7. Prakash, R., Zhang, Y., Feng, W. & Jasin, M. Homologous Recombination and Human Health: The Roles of BRCA1, BRCA2, and Associated Proteins. *Perspectives in Biology* 1–29 (2015) doi:10.1101/cshperspect.a016600.

8. Zelensky, A., Kanaar, R. & Wyman, C. Mediators of Homologous DNA Pairing. *Cold Spring Harb Perspect Biol* **6**, a016451 (2014).

9. Brown, M. S. & Bishop, D. K. DNA strand exchange and RecA homologs in meiosis. *Cold Spring Harb Perspect Biol* **7**, a016659 (2014).

10. Börner, G. V., Kleckner, N. & Hunter, N. Crossover/Noncrossover Differentiation, Synaptonemal Complex Formation, and Regulatory Surveillance at the Leptotene/Zygotene Transition of Meiosis. *Cell* **117**, 29–45 (2004).

11. Pyatnitskaya, A., Borde, V. & De Muyt, A. Crossing and zipping: molecular duties of the ZMM proteins in meiosis. *Chromosoma* **128**, 181–198 (2019).

12. Kneitz, B. *et al.* MutS homolog 4 localization to meiotic chromosomes is required for chromosome pairing during meiosis in male and female mice. *Genes Dev* **14**, 1085–1097 (2000).

13. Edelmann, W. *et al.* Mammalian MutS homologue 5 is required for chromosome pairing in meiosis. *Nat Genet* **21**, 123–127 (1999).

14. de Vries, S. S. *et al.* Mouse MutS-like protein Msh5 is required for proper chromosome synapsis in male and female meiosis. *Genes Dev* **13**, 523–531 (1999).

15. Tarsounas, M., Morita, T., Pearlman, R. E. & Moens, P. B. Rad51 and Dmc1 Form Mixed Complexes Associated with Mouse Meiotic Chromosome Cores and Synaptonemal Complexes. *Journal of Cell Biology* **147**, 207–220 (1999).

16. Slotman, J. A. *et al.* Super-resolution imaging of RAD51 and DMC1 in DNA repair foci reveals dynamic distribution patterns in meiotic prophase. *PLOS Genetics* **16**, e1008595 (2020).

17. Brown, M. S., Grubb, J., Zhang, A., Rust, M. J. & Bishop, D. K. Small Rad51 and Dmc1 Complexes Often Co-occupy Both Ends of a Meiotic DNA Double Strand Break. *PLOS Genetics* **11**, e1005653 (2015).

847 18. Hinch, A. G. *et al.* The Configuration of RPA, RAD51, and DMC1 Binding in Meiosis Reveals the
848 Nature of Critical Recombination Intermediates. *Molecular Cell* (2020)
849 doi:10.1016/j.molcel.2020.06.015.
850 19. Cloud, V., Chan, Y.-L., Grubb, J., Budke, B. & Bishop, D. K. Rad51 is an accessory factor for Dmc1-
851 mediated joint molecule formation during meiosis. *Science (New York, N.Y.)* **337**, 1222–5 (2012).
852 20. Da Ines, O. *et al.* Meiotic Recombination in Arabidopsis Is Catalysed by DMC1, with RAD51 Playing
853 a Supporting Role. *PLoS Genetics* **9**, (2013).
854 21. Halder, S. *et al.* Double-stranded DNA binding function of RAD51 in DNA protection and its
855 regulation by BRCA2. *Molecular Cell* **82**, 3553-3565.e5 (2022).
856 22. Mason, J. M., Chan, Y.-L., Weichselbaum, R. W. & Bishop, D. K. Non-enzymatic roles of human
857 RAD51 at stalled replication forks. *Nat Commun* **10**, 4410 (2019).
858 23. Schlacher, K. *et al.* Double-Strand Break Repair-Independent Role for BRCA2 in Blocking Stalled
859 Replication Fork Degradation by MRE11. *Cell* **145**, 529–542 (2011).
860 24. Berti, M., Cortez, D. & Lopes, M. The plasticity of DNA replication forks in response to clinically
861 relevant genotoxic stress. *Nat Rev Mol Cell Biol* **21**, 633–651 (2020).
862 25. Kolinjivadi, A. M. *et al.* Moonlighting at replication forks – a new life for homologous
863 recombination proteins BRCA1, BRCA2 and RAD51. *FEBS Letters* **591**, 1083–1100 (2017).
864 26. Hashimoto, Y., Ray Chaudhuri, A., Lopes, M. & Costanzo, V. Rad51 protects nascent DNA from
865 Mre11-dependent degradation and promotes continuous DNA synthesis. *Nat Struct Mol Biol* **17**,
866 1305–1311 (2010).
867 27. Reitz, D., Chan, Y.-L. & Bishop, D. K. How strand exchange protein function benefits from ATP
868 hydrolysis. *Curr Opin Genet Dev* **71**, 120–128 (2021).
869 28. Ceballos, S. J. & Heyer, W.-D. Functions of the Snf2/Swi2 family Rad54 motor protein in
870 homologous recombination. *Biochimica et Biophysica Acta (BBA) - Gene Regulatory Mechanisms*
871 **1809**, 509–523 (2011).

872 29. Mason, J. M. *et al.* RAD54 family translocases counter genotoxic effects of RAD51 in human
873 tumor cells. *Nucleic Acids Res* **43**, 3180–3196 (2015).
874 30. Holzen, T. M., Shah, P. P., Olivares, H. A. & Bishop, D. K. Tid1/Rdh54 promotes dissociation of
875 Dmc1 from nonrecombinogenic sites on meiotic chromatin. *Genes Dev.* **20**, 2593–2604 (2006).
876 31. Shah, P. P. *et al.* Swi2/Snf2-Related Translocases Prevent Accumulation of Toxic Rad51
877 Complexes during Mitotic Growth. *Molecular Cell* **39**, 862–872 (2010).
878 32. Li, X. & Heyer, W.-D. RAD54 controls access to the invading 3'-OH end after RAD51-mediated DNA
879 strand invasion in homologous recombination in Saccharomyces cerevisiae. *Nucleic Acids*
880 *Research* **37**, 638–646 (2009).
881 33. Wesoly, J. *et al.* Differential contributions of mammalian Rad54 paralogs to recombination, DNA
882 damage repair, and meiosis. *Mol Cell Biol* **26**, 976–989 (2006).
883 34. Russo, A., Cordelli, E., Salvitti, T., Palumbo, E. & Pacchierotti, F. Rad54/Rad54B deficiency is
884 associated to increased chromosome breakage in mouse spermatocytes. *Mutagenesis* **33**, 323–
885 332 (2018).
886 35. Liu, T., Wan, L., Wu, Y., Chen, J. & Huang, J. hSWS1·SWSAP1 Is an Evolutionarily Conserved
887 Complex Required for Efficient Homologous Recombination Repair *. *Journal of Biological*
888 *Chemistry* **286**, 41758–41766 (2011).
889 36. Prakash, R. *et al.* Distinct pathways of homologous recombination controlled by the SWS1–
890 SWSAP1–SPIDR complex. *Nat Commun* **12**, 4255 (2021).
891 37. Martino, J. *et al.* The human Shu complex functions with PDS5B and SPIDR to promote
892 homologous recombination. *Nucleic acids research* **47**, 10151–10165 (2019).
893 38. Godin, S. K. *et al.* Evolutionary and Functional Analysis of the Invariant SWIM Domain in the
894 Conserved Shu2/SWS1 Protein Family from Saccharomyces cerevisiae to Homo sapiens. *Genetics*
895 **199**, 1023–1033 (2015).
896 39. Martín, V. *et al.* Sws1 is a conserved regulator of homologous recombination in eukaryotic cells.
897 *The EMBO Journal* **25**, 2564–2574 (2006).

898 40. Abreu, C. M. *et al.* Shu complex SWS1-SWSAP1 promotes early steps in mouse meiotic
899 recombination. *Nat Commun* **9**, 3961 (2018).
900 41. Matsuzaki, K., Kondo, S., Ishikawa, T. & Shinohara, A. Human RAD51 paralogue SWSAP1 fosters
901 RAD51 filament by regulating the anti-recombinase FIGNL1 AAA+ ATPase. *Nat Commun* **10**, 1407
902 (2019).
903 42. Huang, T. *et al.* SPIDR is required for homologous recombination during mammalian meiosis.
904 *Nucleic Acids Research* gkad154 (2023) doi:10.1093/nar/gkad154.
905 43. Yuan, J. & Chen, J. FIGNL1-containing protein complex is required for efficient homologous
906 recombination repair. *Proc Natl Acad Sci U S A* **110**, 10640–10645 (2013).
907 44. Fernandes, J. B. *et al.* FIGL1 and its novel partner FLIP form a conserved complex that regulates
908 homologous recombination. *PLoS Genet* **14**, e1007317 (2018).
909 45. Zhang, P. *et al.* The Rice AAA-ATPase OsFIGNL1 Is Essential for Male Meiosis. *Frontiers in Plant*
910 *Science* **8**, (2017).
911 46. Liu, X. *et al.* OsRAD51 Plays a Vital Role in Promoting Homologous Recombination in Rice Meiosis.
912 *International Journal of Molecular Sciences* **23**, 9906 (2022).
913 47. Girard, C. *et al.* AAA-ATPase FIDGETIN-LIKE 1 and Helicase FANCM Antagonize Meiotic Crossovers
914 by Distinct Mechanisms. *PLOS Genetics* **11**, e1005369 (2015).
915 48. Hu, Q. *et al.* Meiotic Chromosome Association 1 Interacts with TOP3α and Regulates Meiotic
916 Recombination in Rice. *The Plant Cell* **29**, 1697–1708 (2017).
917 49. Yang, S. *et al.* FIGNL1 Inhibits Non-homologous Chromosome Association and Crossover
918 Formation. *Frontiers in Plant Science* **13**, (2022).
919 50. Li, X. *et al.* Regulation of interference-sensitive crossover distribution ensures crossover
920 assurance in Arabidopsis. *Proc Natl Acad Sci U S A* **118**, e2107543118 (2021).
921 51. Kumar, R., Duhamel, M., Coutant, E., Ben-Nahia, E. & Mercier, R. Antagonism between BRCA2
922 and FIGL1 regulates homologous recombination. *Nucleic Acids Res* **47**, 5170–5180 (2019).

923 52. Sadate-Ngatchou, P. I., Payne, C. J., Dearth, A. T. & Braun, R. E. Cre recombinase activity specific
924 to post natal, premeiotic male germ cells in transgenic mice. *Genesis* **46**, 738–742 (2008).
925 53. Shi, B. *et al.* Dual functions for the ssDNA-binding protein RPA in meiotic recombination. *PLOS*
926 *Genetics* **15**, e1007952 (2019).
927 54. Imai, Y. *et al.* PRDM9 activity depends on HELLS and promotes local 5-hydroxymethylcytosine
928 enrichment. *Elife* **9**, e57117 (2020).
929 55. Bao, J., Ma, H.-Y., Schuster, A., Lin, Y.-M. & Yan, W. Incomplete cre-mediated excision leads to
930 phenotypic differences between Stra8-iCre; Mov10l1lox/lox and Stra8-iCre; Mov10l1lox/Δ mice.
931 *genesis* **51**, 481–490 (2013).
932 56. Klein, H. L. The consequences of Rad51 overexpression for normal and tumor cells. *DNA Repair*
933 **7**, 686–693 (2008).
934 57. Baudat, F., Manova, K., Yuen, J. P., Jasin, M. & Keeney, S. Chromosome synapsis defects and
935 sexually dimorphic meiotic progression in mice lacking spo11. *Mol Cell* **6**, 989–998 (2000).
936 58. Romanienko, P. J. & Camerini-Otero, R. D. The mouse Spo11 gene is required for meiotic
937 chromosome synapsis. *Mol Cell* **6**, 975–987 (2000).
938 59. Pittman, D. L. *et al.* Meiotic prophase arrest with failure of chromosome synapsis in mice
939 deficient for Dmc1, a germline-specific RecA homolog. *Mol Cell* **1**, 697–705 (1998).
940 60. Yoshida, K. *et al.* The mouse RecA-like gene Dmc1 is required for homologous chromosome
941 synapsis during meiosis. *Mol Cell* **1**, 707–718 (1998).
942 61. Mahadevaiah, S. K. *et al.* Recombinational DNA double-strand breaks in mice precede synapsis.
943 *Nat Genet* **27**, 271-276. (2001).
944 62. Moens, P. B. *et al.* The time course and chromosomal localization of recombination-related
945 proteins at meiosis in the mouse are compatible with models that can resolve the early DNA-
946 DNA interactions without reciprocal recombination. *Journal of Cell Science* **115**, 1611–1622
947 (2002).

948 63. Yoon, S., Choi, E.-H., Kim, J.-W. & Kim, K. P. Structured illumination microscopy imaging reveals
949 localization of replication protein A between chromosome lateral elements during mammalian
950 meiosis. *Exp Mol Med* **50**, 1–12 (2018).
951 64. Yang, F. *et al.* Meiotic failure in male mice lacking an X-linked factor. *Genes Dev.* **22**, 682–691
952 (2008).
953 65. Wassing, I. E. & Esashi, F. RAD51: Beyond the break. *Semin Cell Dev Biol* **113**, 38–46 (2021).
954 66. Koornneef, L. *et al.* Multi-color dSTORM microscopy in Hormad1-/- spermatocytes reveals
955 alterations in meiotic recombination intermediates and synaptonemal complex structure. *PLOS*
956 *Genetics* **18**, e1010046 (2022).
957 67. Carofiglio, F. *et al.* SPO11-independent DNA repair foci and their role in meiotic silencing. *PLoS*
958 *Genet* **9**, e1003538 (2013).
959 68. Khil, P. P., Smagulova, F., Brick, K. M., Camerini-Otero, R. D. & Petukhova, G. V. Sensitive mapping
960 of recombination hotspots using sequencing-based detection of ssDNA. *Genome Res* **22**, 957–
961 965 (2012).
962 69. Brick, K., Smagulova, F., Khil, P., Camerini-Otero, R. D. & Petukhova, G. V. Genetic recombination
963 is directed away from functional genomic elements in mice. *Nature* **485**, 642–645 (2012).
964 70. Lange, J. *et al.* The Landscape of Mouse Meiotic Double-Strand Break Formation, Processing, and
965 Repair. *Cell* **167**, 695-708.e16 (2016).
966 71. Davies, B. *et al.* Re-engineering the zinc fingers of PRDM9 reverses hybrid sterility in mice. *Nature*
967 **530**, 171–176 (2016).
968 72. Pittman, D. L., Weinberg, L. R. & Schimenti, J. C. Identification, characterization, and genetic
969 mapping of Rad51d, a new mouse and human RAD51/RecA-related gene. *Genomics* **49**, 103–111
970 (1998).
971 73. Mercier, R., Mézard, C., Jenczewski, E., Macaisne, N. & Grelon, M. The Molecular Biology of
972 Meiosis in Plants. *Annu. Rev. Plant Biol.* **66**, 297–327 (2015).

74. Petukhova, G. V., Romanienko, P. J. & Camerini-Otero, R. D. The Hop2 Protein Has a Direct Role in Promoting Interhomolog Interactions during Mouse Meiosis. *Developmental Cell* **5**, 927–936 (2003).

75. Pezza, R. J., Petukhova, G. V., Ghirlando, R. & Camerini-Otero, R. D. Molecular activities of meiosis-specific proteins Hop2, Mnd1, and the Hop2-Mnd1 complex. *J Biol Chem* **281**, 18426–18434 (2006).

76. Zhao, W. & Sung, P. Significance of ligand interactions involving Hop2-Mnd1 and the RAD51 and DMC1 recombinases in homologous DNA repair and XX ovarian dysgenesis. *Nucleic Acids Research* **43**, 4055–4066 (2015).

77. Finsterbusch, F. *et al.* Alignment of Homologous Chromosomes and Effective Repair of Programmed DNA Double-Strand Breaks during Mouse Meiosis Require the Minichromosome Maintenance Domain Containing 2 (MCMDC2) Protein. *PLOS Genetics* **12**, e1006393 (2016).

78. McNairn, A. J., Rinaldi, V. D. & Schimenti, J. C. Repair of Meiotic DNA Breaks and Homolog Pairing in Mouse Meiosis Requires a Minichromosome Maintenance (MCM) Paralog. *Genetics* **205**, 529–537 (2017).

79. Lutzmann, M. *et al.* MCM8- and MCM9-deficient mice reveal gametogenesis defects and genome instability due to impaired homologous recombination. *Mol Cell* **47**, 523–534 (2012).

80. Hustedt, N. *et al.* Control of homologous recombination by the HROB–MCM8–MCM9 pathway. *Genes Dev.* **33**, 1397–1415 (2019).

81. Cole, F. *et al.* Mouse tetrad analysis provides insights into recombination mechanisms and hotspot evolutionary dynamics. *Nat Genet* **46**, 1072–1080 (2014).

82. Piazza, A. & Heyer, W.-D. Moving forward one step back at a time: reversibility during homologous recombination. *Curr Genet* **65**, 1333–1340 (2019).

83. Yu, D. S. *et al.* Dynamic Control of Rad51 Recombinase by Self-Association and Interaction with BRCA2. *Molecular Cell* **12**, 1029–1041 (2003).

84. Lan, W.-H. *et al.* Rad51 facilitates filament assembly of meiosis-specific Dmc1 recombinase. *Proceedings of the National Academy of Sciences* **117**, 11257–11264 (2020).

85. Viera, A. *et al.* PDS5 proteins regulate the length of axial elements and telomere integrity during male mouse meiosis. *EMBO reports* **21**, e49273 (2020).

86. Stok, C. *et al.* The FIGNL1-interacting protein C1orf112 is synthetic lethal with PICH and mediates RAD51 retention on chromatin. 2022.10.07.511242 Preprint at https://doi.org/10.1101/2022.10.07.511242 (2022).

87. Rinaldi, V. D., Bolcun-Filas, E., Kogo, H., Kurahashi, H. & Schimenti, J. C. The DNA Damage Checkpoint Eliminates Mouse Oocytes with Chromosome Synapsis Failure. *Mol Cell* **67**, 1026-1036.e2 (2017).

88. Ravindranathan, R., Raveendran, K., Papanikos, F., San-Segundo, P. A. & Tóth, A. Chromosomal synapsis defects can trigger oocyte apoptosis without elevating numbers of persistent DNA breaks above wild-type levels. *Nucleic Acids Res* **50**, 5617–5634 (2022).

89. Bolcun-Filas, E. *et al.* Mutation of the Mouse Syce1 Gene Disrupts Synapsis and Suggests a Link between Synaptonemal Complex Structural Components and DNA Repair. *PLOS Genetics* **5**, e1000393 (2009).

90. Crichton, J. H., Dunce, J. M., Baarends, W. M., Davies, O. R. & Adams, I. R. Parallel recruitment pathways contribute to synaptonemal complex assembly during mammalian meiosis. 2022.04.14.488335 Preprint at https://doi.org/10.1101/2022.04.14.488335 (2022).

91. Couturier, A. M. *et al.* Roles for APRIN (PDS5B) in homologous recombination and in ovarian cancer prediction. *Nucleic Acids Research* **44**, 10879–10897 (2016).

92. Morales, C. *et al.* PDS5 proteins are required for proper cohesin dynamics and participate in replication fork protection. *Journal of Biological Chemistry* **295**, 146–157 (2020).

93. Xu, H. *et al.* Molecular organization of mammalian meiotic chromosome axis revealed by expansion STORM microscopy. *Proceedings of the National Academy of Sciences* **116**, 18423–18428 (2019).

1024 94. Schwenk, F., Baron, U. & Rajewsky, K. A cre -transgenic mouse strain for the ubiquitous deletion
1025 of loxP -flanked gene segments including deletion in germ cells. *Nucleic Acids Research* **23**, 5080–
1026 5081 (1995).
1027 95. Abreu, C. M. *et al.* Shu complex SWS1-SWSAP1 promotes early steps in mouse meiotic
1028 recombination. *Nat Commun* **9**, 3961 (2018).
1029 96. Peters, A. H., Plug, A. W., van Vugt, M. J. & de Boer, P. A drying-down technique for the spreading
1030 of mammalian meiocytes from the male and female germline. *Chromosome research* **5**, 66–8
1031 (1997).
1032 97. Grey, C., Baudat, F. & Massy, B. de. Genome-Wide Control of the Distribution of Meiotic
1033 Recombination. *PLOS Biology* **7**, e1000035 (2009).
1034 98. Schindelin, J. *et al.* Fiji: an open-source platform for biological-image analysis. *Nat Methods* **9**,
1035 676–682 (2012).
1036 99. Lachmanovich, E. *et al.* Co-localization analysis of complex formation among membrane proteins
1037 by computerized fluorescence microscopy: application to immunofluorescence co-patching
1038 studies. *Journal of Microscopy* **212**, 122–131 (2003).
1039 100. Grey, C. *et al.* In vivo binding of PRDM9 reveals interactions with noncanonical genomic sites.
1040 *Genome research* **27**, 580–590 (2017).
1041 101. Brick, K., Pratto, F., Sun, C.-Y., Camerini-Otero, R. D. & Petukhova, G. Chapter Sixteen - Analysis
1042 of Meiotic Double-Strand Break Initiation in Mammals. in *Methods in Enzymology* (eds. Spies, M.
1043 & Malkova, A.) vol. 601 391–418 (Academic Press, 2018).
1044 102. Li, Q., Brown, J. B., Huang, H. & Bickel, P. J. Measuring reproducibility of high-throughput
1045 experiments. *The Annals of Applied Statistics* **5**, 1752–1779 (2011).
1046 103. Ramírez, F. *et al.* deepTools2: a next generation web server for deep-sequencing data analysis.
1047 *Nucleic Acids Research* **44**, W160–W165 (2016).

104. Gomes, X. V., Henricksen, L. A. & Wold, M. S. Proteolytic mapping of human replication protein A: Evidence for multiple structural domains and a conformational change upon interaction with single-stranded DNA. *Biochemistry* **35**, 5586–5595 (1996).

105. Veaute, X. *et al.* The Srs2 helicase prevents recombination by disrupting Rad51 nucleoprotein filaments. *Nature* **423**, 309–312 (2003).

106. Dubochet, J., Ducommun, M., Zollinger, M. & Kellenberger, E. A new preparation method for dark-field electron microscopy of biomacromolecules. *Journal of ultrastructure research* **35**, 147–67 (1971).

Supplementary Table 1. Primers used for mouse genotyping

Primer	Sequence (5'-3')	Genotype: amplicon
Firrm wild-type and floxed allele, forward	CTTGGCTCGCTTTGCTTTGA	WT: 304bp
Firrm wild-type and floxed allele, reverse	TGTAGTTTACATCTTCCCTATGACA	*Firrm*^{fl}: ~500bp
		Firrm^{-}: -
Firrm floxed and deleted allele, forward	AAGGCGCATAACGATACCAC	WT: -
Firrm floxed and deleted allele, reverse	ACTGATGGCGAGCTCAGACC	*Firrm*^{fl}: ~1kb
		Firrm^{-}: 178bp
Fignl1 wild-type and floxed allele, forward	GGGATCAAACACTAGGGTTCAGGC	WT: 200bp
Fignl1 wild-type and floxed allele, reverse	GATACAGTCTTCAAGATTAAGGACAACC	*Fignl1*^{fl}: 400bp
		Fignl1^{-}: -
Fignl1 deleted allele, forward	GGGATCAAACACTAGGGTTCAGGC	WT: -
Fignl1 deleted allele, reverse	CGGGTTACGGTAGTTTACTCCC	*Fignl1*^{fl}: -
		Fignl1^{-}: 412bp
Stra8-Cre transgenic allele, forward	GTGCAAGCTGAACAACAGGA	No transgene: -
Stra8-Cre transgenic allele, reverse	AGGGACACAGCATTGGAGTC	*Stra8-Cre*: ~150bp
Cmv-Cre transgenic allele, forward	TGGGCGGCATGGTGCAAGTT	No transgene: -
Cmv-Cre transgenic allele, reverse	CGGTGCTAACCAGCGTTTTC	*Cmv-Cre*: 466bp
Spo11 wild-type and YF allele, forward	CTGGTCGATGCAGATCCCTACGG	WT: 394bp
Spo11 wild-type and YF allele, reverse	TAGATGCACATTATCTCGATGCC	*Spo11*^{YF}: 482bp
Swsap1 wild-type and deleted allele, forward	TCTGTGAACTATAGCCAATGAGGC	WT: 396bp
Swsap1 wild-type and deleted allele, reverse	AACTGTCACTCAGGCGCGAACTAG	*Swsap1*$^{-}$: 265bp

Supplementary Table 2. List of antibodies used in this study

Antibody	Source	Identifier/Reference	Application	Dilution
Guinea-pig anti-SYCP3	home made	DOI: 10.1371/journal.pbio.1000035	IF, WB	1:500, 1:3000
Mouse anti-SYCP3	Abcam	ab97672	IF	1:200
Rabbit anti-SYCP1	Abcam	ab15090	IF	1:400
Mouse anti-γH2AX	Millipore	05-636-I	IF	1:10000
Guinea-pig anti-SYCP1	from H. Cook		IF	1:200
Rabbit anti-MSH4	Abcam	ab58666	IF	1:200
Rabbit anti-RPA2	Abcam	ab76420	IF	1:200
Rat anti-RPA2	Cell Signaling	2208	IF	1:200
Rabbit anti-DMC1	Santa Cruz	sc-22768	IF, WB	1:200, 1:1000
Guinea-pig anti-DMC1	from Prof. Qinghua Shi	DOI: 10.1016/j.molcel.2020.06.015	IF	1:100
Goat anti-DMC1	Santa Cruz	sc-8973	ChIP	
Rabbit anti-RAD51	Calbiochem	PC130	IF, WB	1:500, 1:1000
Rabbit anti-FIGNL1	Proteintech	17604-1-AP	WB	1:500
Rabbit anti-C1orf112 (anti-hFIRRM)	Abcam	ab121774	WB	1:500
Rabbit anti-beta Tubulin	Abcam	ab6046	WB	1:3000
Goat anti-rabbit A488	Molecular Probes	A-21206	IF	1:400
Goat anti-rabbit A555	Molecular Probes	A-21248	IF	1:400
Goat anti-rabbit Star Orange	Abberior GMBH	STORANGE-1002-5	IF -STED	1:100
Goat anti-guinea pig Cy3	Jackson	706-165-148	IF	1:400
Goat anti-guinea pig Cy5	Jackson	706-175-148	IF	1:400
Goat anti-guinea pig Star Red	Abberior GMBH	STRED-1006-500U	IF-STED	1:100
Donkey anti-rat A555	ThermoFisher	A48270	IF	1:400
Goat anti-rat Star Red	Abberior GMBH	STRED-1007-500U	IF-STED	1:100
Donkey anti-mouse A647	Thermo Fisher	ab150107	IF	1:400
Goat anti-mouse Star Green	Abberior GMBH	STGREEN-1001-50	IF-STED	1:100
Anti-rabbit HRP	Jackson Immunoresearch	711-035-152	WB	1:5000
Donkey anti-guinea pig HRP	Jackson Immunoresearch	706-035-148	WB	1:5000

IF, immunofluorescence; WB, western blotting; ChIP, chromatin immunoprecipitation

Figure Legends

Figure 1a. Testis weight relative to body weight in control (n=24), *Firrm* cKO (n=15), *Fignl1* cKO (n=4) and *Firrm* cKO *Fignl1* cKO (n=1) adult mice (30 dpp to 95 dpp). Unpaired t-test, two-sided. **b.** Periodic acid-Schiff-stained testis sections from adult mice of the indicated genotypes. Spg, spermatogonia; Spc, spermatocytes; rSpt, round spermatids; eSpt, elongated spermatids. Scale bar, 40 µm. **c.** Western blot analysis of cytoplasmic (80µg) and nuclear (100µg) fractions from testes of 12 dpp mice of the indicated genotypes. **d.** Chromosome axes (SYCP3, red) and synaptonemal complex (SYCP1, green) were detected in spread leptotene, early zygotene (control) or zygotene-like (cKO), and pachytene (control) or late zygotene-like (cKO) spermatocyte nuclei from control, *Firrm* cKO and *Fignl1* cKO mice. Scale bar, 10 µm. **e.** Distribution of spermatocytes at different meiotic prophase substages in juvenile *Firrm* cKO mice (indicated age) and in adult (8-week-old) *Fignl1* cKO mice. Chi-square test. For all figures: ns, non-significant; *0.01< p ≤0.05; **0.001< p ≤0.01; ***0.0001< p ≤0.001; ****p ≤0.0001.

Figure 2. Early recombination events are normal in *Firrm* cKO and *Fignl1* cKO spermatocytes.
a. Representative images of spread nuclei of pre-leptotene, early leptotene and leptotene spermatocytes from control and *Firrm* cKO mice stained for SYCP3 and γH2AX. Scale bar, 20 µm. **b.** Total nuclear γH2AX signal intensity in control (gray) and *Firrm* cKO (red) spermatocytes (n=2 mice per genotype). **c.** Representative images of spread spermatocyte nuclei from 12 dpp control and *Firrm* cKO mice stained for SYCP3 and RPA2. Scale bar, 10 µm. **d.** Number of on-axis RPA2 foci in control (gray), *Firrm* cKO (red) and *Fignl1* cKO (orange) spermatocytes. Mann-Whitney two-tailed test; n=5 (control), n=4 (*Firrm* cKO) and n=2 (*Fignl1* cKO) mice per genotype.

Figure 3. *Firrm* cKO and *Fignl1* cKO spermatocytes accumulate RAD51 and DMC1, and are deficient for later meiotic HR intermediates. a. Representative images of zygotene spermatocyte spreads from control and *Firrm* cKO mice stained for SYCP3, RAD51 and DMC1. Scale bar, 5 µm. **b, c.** Numbers of RAD51 **(b)** and DMC1 **(c)** foci in control and *Firrm* cKO **(b)**, and in control, *Firrm* cKO and *Fignl1* cKO spermatocytes **(c)**. n=2 mice per genotype, except for RAD51 foci in *Fignl1* cKO (n=1). **d.** Representative spreads of zygotene spermatocytes from 16 dpp control, *Firrm* cKO and $Spo11^{YF/YF}$ mice stained with SYCP3, SYCP1 and MSH4. Scale bar, 10 µm. **e.** MSH4 focus density along SYCP1-marked synaptonemal complex fragments in control, *Firrm* cKO, $Spo11^{YF/YF}$ *Firrm* cKO, and $Spo11^{YF/YF}$ zygotene/zygotene-like spermatocytes. Mann-Whitney two-tailed test. n=3 mice per genotype. **f.** Preleptotene spermatocyte spreads from control and *Firrm* cKO mice stained for SYCP3, RPA2 (red) and RAD51 (green). Scale bar, 10 µm. **g.** STED images of preleptotene spermatocyte spreads from control and *Firrm* cKO mice stained

for RAD51 (STAR ORANGE, green) and RPA2 (STAR RED, red). Scale bar, 1 µm. **h-i.** Number of RAD51 foci that colocalized with RPA2 foci **(h)** and of RPA2 foci that colocalized with RAD51 **(i)** in spreads of preleptotene control and *Fignl1* cKO spermatocyte nuclei (n=1 mouse per genotype)**.** The observed (obs) and expected by chance (random) numbers of colocalized foci are shown. Mann-Whitney two-tailed test.

Figure 4. RAD51 and DMC1 patterns in mouse meiotic chromosomes. a-c. Number **(a)** of on-axis RAD51 foci that colocalized with on-axis DMC1 foci, and vice-versa, in spreads from control and *Firrm* cKO spermatocytes from 12 dpp mice. The observed (obs) and expected by chance (random) numbers of RAD51 foci that colocalized with DMC1 are shown in **(a)**. Random, average of 100 simulations where the colocalization of randomly distributed DMC1 foci with actual RPA2 foci was measured. Wilcoxon two-tailed test. **b,c.** Percentage (corrected for random colocalization, see Methods) of on-axis RAD51 foci colocalized with on-axis DMC1 foci **(b)** and vice-versa **(c)**. There were not enough on-axis RAD51 and DMC1 foci in early leptotene control spermatocytes to measure colocalization reliably. Mann-Whitney two-tailed test. **d.** STED images of spreads of leptotene spermatocyte nuclei stained for SYCP3 (STAR GREEN, white), RAD51 (STAR ORANGE, green), and DMC1 (STAR RED, red). **e.** STED images of spreads of zygotene/zygotene-like spermatocyte nuclei with extensive synaptonemal complexes, stained for SYCP3 (STAR 460L, white), RAD51 (STAR RED, red) and DMC1 (STAR ORANGE, green). **f.** Relative intensity of SYCP3 (black), RAD51 (red) and DMC1 (green) signal across the synaptonemal complex in control (across RAD51-DMC1 mixed foci) and *Firrm* cKO (outside regions of stronger focus-like RAD51-DMC1 staining). Data are the mean of 12 sections from STED images of 3 different nuclei.

Figure 5. FIRRM prevents DSB-independent accumulation of RAD51 and DMC1 in mouse spermatocyte chromosomes. a. Spreads of representative control, *Firrm* cKO, *Spo11*$^{YF/YF}$ *Firrm* cKO, and *Spo11*$^{YF/YF}$ early zygotene spermatocytes stained for SYCP3, DMC1 and RAD51. Scale bar, 10 µm. **b-c.** Counts of on-axis RAD51 **(b)** and DMC1 **(c)** foci in spreads from control, *Firrm* cKO, *Spo11*$^{YF/YF}$ *Firrm* cKO, and *Spo11*$^{YF/YF}$ spermatocytes from 12 dpp mice. Foci overlapping with (on-axis, top panels) or outside (Extended Data Figure 4c-d) chromosome axes, defined by the SYCP3 signal, were counted separately. Mann-Whitney two-tailed test. n=2 mice per genotype.

Figure 6. DMC1 is recruited at meiotic DSB hotspots in *Firrm* cKO spermatocytes. a-b. Percentages of on-axis RPA2 foci colocalized with on-axis DMC1 foci **(a)**, and of DMC1 foci colocalized with RPA2 **(b)** in spreads from early leptotene to mid-zygotene/zygotene-like spermatocyte nuclei from control and *Firrm* cKO mice. Mann-Whitney two-tailed test. **c.** Numbers of and shared hotspots identified by DMC1-SSDS in spermatocytes from 12 dpp control and *Firrm* cKO mice. **d**. DMC1-SSDS signal

correlation between control and *Firrm* cKO mice at hotspots identified in both genotypes. The Spearman rho and associated p-value (two-sided) are shown. Red and green dots indicate hotspots that were significantly over- and under-represented in *Firrm* cKO compared with control spermatocytes (DESeq2, p-value <0.1, log2FC >0 and log2FC <0, respectively). Unchanged autosomal hotspots are represented in gray and chromosome X hotspots by black circled diamonds. **e**. Average plots (top) and corresponding heatmaps (bottom) of DMC1-SSDS intensity (fragments per million, FPM) in control (left) and *Firrm* cKO mice (right) for hotspots that overlap with SPO11-oligo hotspots [70] detected in both genotypes (common peaks), in control only (control-specific), or in *Firrm* cKO only (*Firrm* cKO-specific)(see Extended Data Fig. 7a). The center of intervals is defined as the center of SPO11-oligo peaks detected in B6 mice, as defined in (Lange, 2016). **f.** Normalized average distribution of ssDNA type 1 fragments (see Methods) originating from forward (fwd) and reverse strands (rev) at common peaks, defined in **(e)**, for control (red, orange) and *Firrm* cKO (blue, light blue). The SSDS signal was normalized to have the same cumulated amount of normalized signal from both forward and reverse strands over common peaks (on 5-kb windows) for both genotypes.

Figure 7. *Firrm* and *Fignl1* deletion restore RAD51 and DMC1 loading in *Swsap1*$^{-/-}$ spermatocytes. a. Spreads of control, *Firrm* cKO, *Swsap1*$^{-/-}$ *Firrm* cKO ,and *Swsap1*$^{-/-}$ early zygotene spermatocytes stained for SYCP3 (gray), RAD51 (yellow) and RPA2 (magenta). Scale bar, 10 µm. **b-d.** Numbers of on-axis RPA2 **(b)**, RAD51 **(c)** and DMC1 **(d)** foci in spreads from control, *Fignl1* cKO, and *Swsap1*$^{-/-}$ *Fignl1* cKO spermatocytes from 17 dpp mice. Mann-Whitney two-tailed test. n=1 mouse per genotype. **e-f.** Percentage of on-axis RPA2 foci colocalized with on-axis RAD51 **(e)** or DMC1 **(f)** foci on spreads from control, *Fignl1* cKO, and *Swsap1*$^{-/-}$ *Fignl1* cKO spermatocytes from 17dpp mice. The numbers of colocalized foci were corrected for the numbers expected by chance (see Methods).

Figure 8. FIGLN1 alters the architecture and the activity of RAD51 and DMC1 nucleoprotein filaments. a-b. Electrophoretic Mobility Shift Assay (EMSA). 1 µM RAD51 or DMC1 was incubated (20 minutes) with 3 µM (nucleotide concentration) of a Cy5-labeled 400 nt ssDNA fragment **(a)** or a Cy5-labeled 200 bp dsDNA fragment **(b)** with or without 1.6 µM human FIGNL1ΔN. For the pre-formed nucleofilament panels, RAD51 or DMC1 was incubated with DNA for 5 minutes before adding FIGNL1ΔN for 15 minutes. For the no pre-formed filament panels, RAD51 or DMC1 was added to the reaction concomitantly with FIGNL1ΔN. **c.** Quantification of free dsDNA in the EMSA performed with dsDNA and without pre-formed nucleofilament shown in **(b).** n=2 per condition. Paired t-test, two-sided. **d-f**. Representative TEM images in positive **(d)** and negative staining **(e)** and length distribution **(f)** of RAD51 filaments assembled on 400 nt ssDNA fragments (ss400) without (left, ss400-RAD51) or with human FIGNL1ΔN (right, ss400-RAD51 + FIGNL1ΔN). Some very long filaments (>450nm) that

formed in the presence of FIGNL1ΔN **(d)** were not included in the quantification in **(f)** (see Extended Data Fig. 9b). **g-h**. FIGNL1ΔN inhibits the formation of a D-loop by RAD51 and DMC1 *in vitro*. Representative gel (RAD51 in the presence of increasing concentrations of FIGNL1ΔN, from 0.4 to 1.6 µM) **(g)**. Titration of FIGNL1ΔN **(h)** in the D-loop assay. **i.** Model for possible (and non-exclusive) roles of the FIGNL1-FIRRM complex in regulating RAD51 and DMC1 in mouse spermatocytes. (i) The FIGNL1-FIRRM complex may limit the nuclear RAD51 level by sequestering a cytoplasmic RAD51 pool, possibly by promoting RAD51 polymerization, thus preventing its mobilization by BRCA2. (ii) The FIGNL1-FIRRM complex might prevent the stabilization of transient dsDNA-RAD51 association at replication forks during premeiotic replication. (iii) During meiotic recombination, the FIGNL1-FIRRM complex might first promote indirectly the polymerization of a continuous DMC1 filament on the meiotic DSB 3' ssDNA overhang by preventing the loading of stable RAD51 patches on the 3' region of the ssDNA tails. This would allow the 5' to 3' polymerization of DMC1 (arrows) up to the 3' ends. A factor (e.g., the SWSAP1-SWS1-SPIDR complex) may protect the RAD51 filament from FIGNL1-FIRRM-dependent dissociation in the dsDNA-proximal region of ssDNA tails. The formation of shorter/patchy DMC1 filaments in the absence of the FIGL1-FIRRM complex might not be fully functional for homology search, strand invasion and D-loop stabilization. Post-strand invasion, the FIGNL1-FLIP complex might also be involved in removing RAD51/DMC1 from invading ends involved in intersister (not shown) and/or interhomolog interactions.

Extended Fig. 1. Structure of Firrm and Fignl1 cKO alleles. a. Genomic structure of the floxed and knockout (KO) *Firrm* and *Fignl1* alleles. Open boxes, coding exons; gray-filled boxes, non-coding exons**. b.** The mouse FIRRM protein. The conserved DUF4487 domain is indicated, with the position of exon 7 deleted in the KO (generating a frameshift), and the following internal methionine (M, position 406).

Extended Fig. 2. Increased RAD51 and DMC1 loading, and defective MSH4 and TEX11 focus formation, in *Firrm* cKO and *Fignl1* cKO spermatocytes. a. Representative images of pre-leptotene to late zygotene spermatocyte spreads from control and *Firrm* cKO mice stained for SYCP3, RAD51 and DMC1. Scale bar, 10 µm. **2b.** Spreads of zygotene spermatocytes from 16 dpp control and *Firrm* cKO mice stained with SYCP3 and TEX11. **c.** Number of MSH4 foci along SYCP1-marked synaptonemal complex fragments in control, *Firrm* cKO, *Spo11*$^{YF/YF}$ *Firrm* cKO, and *Spo11*$^{YF/YF}$ zygotene or zygotene-like spermatocytes. The number of MSH4 foci varied with the SC length in control and *Firrm* cKO spermatocytes. The linear regression fit is shown, with the standard error. **d.** Numbers of off-axis RPA2 foci in control (gray), *Firrm* cKO and *Fignl1* cKO spermatocytes (red). Mann-Whitney two-tailed test. n=3 (control) and n=2 (*Firrm* cKO and *Fignl1* cKO) mice per genotype. **e.** Numbers of all and of colocalized RAD51 (green) and RPA2 (red) foci in spreads of preleptotene control and *Fignl1* cKO

spermatocyte nuclei (n=1 mouse per genotype)**.** The numbers of colocalized foci were corrected for the number of colocalized foci expected by chance (see Methods). Mann-Whitney two-tailed test.

Extended Fig. 3. Colocalization of on- and off-axis DMC1 and RAD51 foci in *Firrm* cKO spermatocytes. **a.** Number of on-axis DMC1 foci colocalized with on-axis RAD51 foci from early leptotene to mid-zygotene/zygotene-like stage in control and *Firrm* cKO spread spermatocyte nuclei from 12 dpp mice. The observed (obs) and expected by chance (random) numbers of RAD51 foci colocalized with DMC1 are shown. obs, number of detected colocalized foci. Random, average of 100 simulations where the colocalization of randomly distributed RAD51 foci with actual RPA2 foci was measured. Wilcoxon two-tailed test**. b, c.** Number of off-axis RAD51 foci colocalized with off-axis DMC1 foci **(b)** and number of off-axis DMC1 foci colocalized with off-axis RAD51 foci **(c)** from preleptotene to mid-zygotene/zygotene-like in spread spermatocyte nuclei from 12 dpp control and *Firrm* cKO mice. **d, e**. Percentage of RAD51 foci colocalized with DMC1 **(d)**, and of DMC1 foci colocalized with RAD51 **(e)**, corrected for random colocalization. Mann-Whitney two-tailed test.

Extended Fig. 4. Meiotic DSBs do not form in *Spo11$^{YF/YF}$ Firrm* cKO spermatocytes. Representative spread nuclei of spermatocytes from control, *Firrm* cKO, *Spo11$^{YF/YF}$ Firrm* cKO, and *Spo11$^{YF/YF}$* mice stained for SYCP3, SYCP1 and γH2AX **(a)** or for SYCP3 and RPA2 **(b)**. Scale bar, 10 µm.

Extended Fig. 5. SPO11 DSB-independent DMC1 and RAD51 foci colocalize in *Spo11$^{YF/YF}$ Firrm* cKO spermatocytes. a-f. Numbers of off-axis RAD51 **(a)** and DMC1 **(b)** foci for control, *Firrm* cKO, *Spo11$^{YF/YF}$ Firrm* cKO, and *Spo11$^{YF/YF}$* spermatocyte spreads. n=2 mice per genotype. Mann-Whitney two-tailed test **c-f.** Number **(c-d)** and percentage (corrected for random colocalization) **(e-f),** of on-axis RAD51 foci colocalized with on-axis DMC1 foci **(c,e)** and vice-versa **(d,f),** from early leptotene to mid-zygotene/zygotene-like on spread from spermatocytes of 12 dpp control, *Firrm* cKO, *Spo11$^{YF/YF}$ Firrm* cKO, and *Spo11$^{YF/YF}$* mice. n=2 mice per genotype.

Extended Fig. 6. Similar numbers of DMC1 and RPA foci colocalize in wild-type and *Firrm* cKO spermatocytes. a-b. Number of on-axis DMC1 foci colocalized with on-axis RPA2 foci on spreads from early leptotene to mid-zygotene/zygotene-like spermatocyte nuclei from control and *Firrm* cKO mice. The observed (obs) and expected by chance (random) numbers of DMC1 foci colocalized with RPA2 are shown in **(a)**, while the counts are corrected for the number expected by chance in **(b)**. obs, number of detected colocalizing foci. Random, average of 100 simulations where the colocalization of randomly distributed DMC1 foci with actual RPA2 foci was measured. Wilcoxon two-tailed test **(a)**. Mann-Whitney two-tailed test **(b)**. **c-f.** Number **(c-d)** and percentages **(e-f)** of on-axis DMC1 foci colocalized

with on-axis RPA2 foci on spreads from early leptotene to mid-zygotene/zygotene-like spermatocyte nuclei from control and *Fignl1* cKO mice. The observed (obs) and expected by chance (random) counts of DMC1 foci colocalized with RPA2 are shown in **(c)**, while the counts were corrected for the number expected by chance in **(d)**. obs, number of observed colocalizing foci. Random, average of 100 simulations where the colocalization of randomly distributed on-axis DMC1 foci with actual on-axis RPA2 foci was measured. Wilcoxon two-tailed test. **e, f**. Percentage (corrected for random colocalization) of DMC1 foci colocalized with RPA2 **(e)**, and of RPA2 foci colocalized with DMC1 **(f)**. Mann-Whitney two-tailed test.

Extended Fig. 7. DMC1 recruitment at meiotic DSB hotspots in *Firrm* cKO spermatocytes. a. Numbers and overlap of hotspots identified by DMC1-SSDS in spermatocytes from 12 dpp control and *Firrm* cKO mice, and of SPO11-oligo hotspots detected in C57BL/6J mice in [70]. **b-c**. Average plots (top) and corresponding heatmaps (bottom) of DMC1-SSDS signal in control and *Firrm* cKO mice (2 biological replicates/each), at all common, control-specific, and *Firrm* cKO-specific DMC1 hotspots identified in our analysis **(b)**, and at hotspots overlapping with SPO11-oligo hotspots detected in C57BL/6J mice **(c)**. In **(c)**, the center of the intervals was the center of SPO11-oligo peaks detected in B6 mice, as defined in (Lange, 2016). **d.** Average DMC1-SSDS signal distribution at common DMC1 hotspots, defined in **(c)**, at autosomal hotspots (left panel) and at X and Y chromosome hotspots (right panel), for control (blue) and *Firrm* cKO (red). The DMC1-SSDS signal was normalized to have the same total amount of normalized signal for all common hotspots (on 5-kb windows) in both genotypes. The relative excess of DMC1-SSDS signal at X-Y chromosome hotspots in control is clear. **e.** Average plots of DMC1-SSDS signal intensity (in FPM) at common hotspots defined in **(c)**, ranked within 5 bins of decreasing intensity.

Extended Fig. 8. *Fignl1* deletion restores the formation of RAD51 and DMC1 loading in *Swsap1*$^{-/-}$ spermatocytes. a-c. Numbers of off-axis RPA2 **(a)**, RAD51 **(b)** and DMC1 **(c)** foci detected on spermatocyte spreads from 17 dpp control, *Fignl1* cKO, and *Swsap1*$^{-/-}$ *Fignl1* cKO mice. Mann-Whitney two-tailed test. n=1 mouse per genotype. **d-g.** Numbers **(d-e)** or percentages **(f-g)** of on-axis RAD51 **(d,f)**, and DMC1 **(e,g)** foci colocalized with on-axis RPA2 foci in spermatocyte spreads from 17 dpp control, *Fignl1* cKO, and *Swsap1*$^{-/-}$ *Fignl1* cKO mice. The numbers of colocalized foci were corrected to the number expected by chance (see Methods). Mann-Whitney two-tailed test. n=1 mouse per genotype.

Extended Fig. 9. FIGLN1 alters the architecture and the activity of RAD51 and DMC1 nucleoprotein filaments. a. Purification of recombinant Histidine-tagged human FIGNL1ΔN284 protein from *E. coli*.

Top panel, SDS-page analysis of proteins in total protein lysate (L), soluble protein fraction (S), flow-through (FT) from Hi-trap column, wash, and elution fractions (E1 to E7). Bottom panel, SDS-PAGE analysis of protein fractions collected during the gel filtration purification. Fractions E3, E4, and E5 from previous step were pooled and are shown as input control. Red arrows indicate recombinant His-FIGNL1ΔN284 with an expected size of 46kDa. F11 and F12 fractions were used for biochemical assays in this study. **b.** Length distribution of RAD51 filaments formed on 400 nt ssDNA fragments without (ss400-RAD51) or with (ss400-RAD51+ FIGNL1ΔN) 1.6 µM human FIGNL1ΔN. Note the presence of >450nm-long filaments when FIGNL1ΔN is present that were not included in the quantification shown in Figure 8f. **c.** Representative TEM images of RAD51 in the presence of ATP but in the absence of DNA (negative staining, left), and in presence of human FIGNL1ΔN (negative staining, scale bar 100nm, top right panel; and positive staining, scale bar 500nm, bottom panel). Note the presence of long filaments despite the absence of DNA. **d.** Representative TEM images (negative staining) of DMC1 filaments assembled on a 400 bp dsDNA (top) or 400 nt ssDNA (bottom) fragment, without (left) or with human FIGNL1ΔN (right). Scale bar, 100 nm.

Source Data. a-b. Uncropped image of the gels shown in Fig. 8a-b. Unlabeled lanes are not displayed on the final figure.

Figure 1

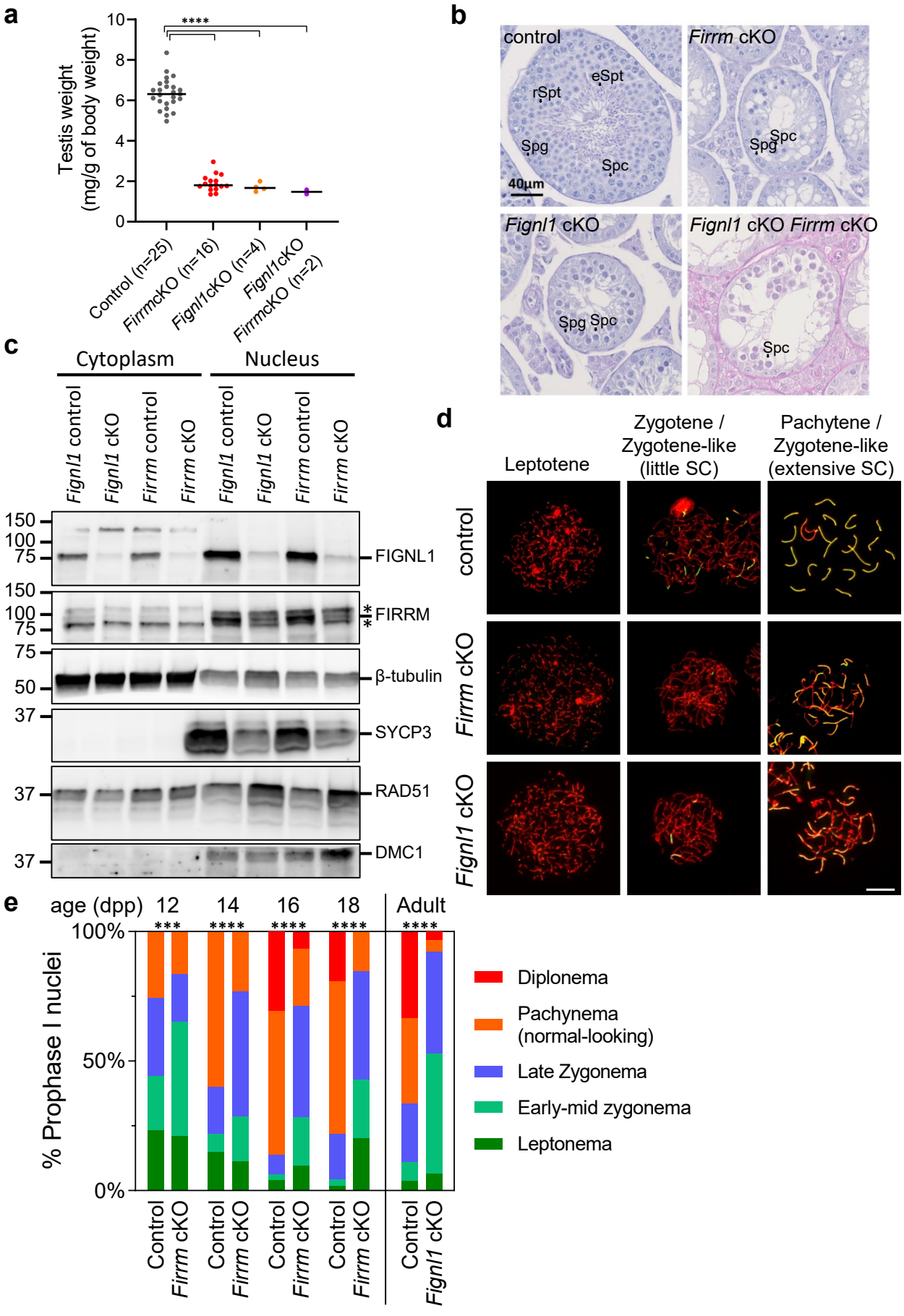
a
Testis weight (mg/g of body weight)
****
Control (n=25)
FirrmcKO (n=16)
Fignl1cKO (n=4)
Fignl1cKO FirrmcKO (n=2)
b
control
Firrm cKO
Fignl1 cKO
Fignl1 cKO Firrm cKO
eSpt
rSpt
Spg
Spc
40µm
c
Cytoplasm
Nucleus
Fignl1 control
Fignl1 cKO
Firrm control
Firrm cKO
FIGNL1
FIRRM
β-tubulin
SYCP3
RAD51
DMC1
d
Leptotene
Zygotene / Zygotene-like (little SC)
Pachytene / Zygotene-like (extensive SC)
control
Firrm cKO
Fignl1 cKO
e
age (dpp)
12
14
16
18
Adult
% Prophase I nuclei
Diplonema
Pachynema (normal-looking)
Late Zygonema
Early-mid zygonema
Leptonema

Figure 2

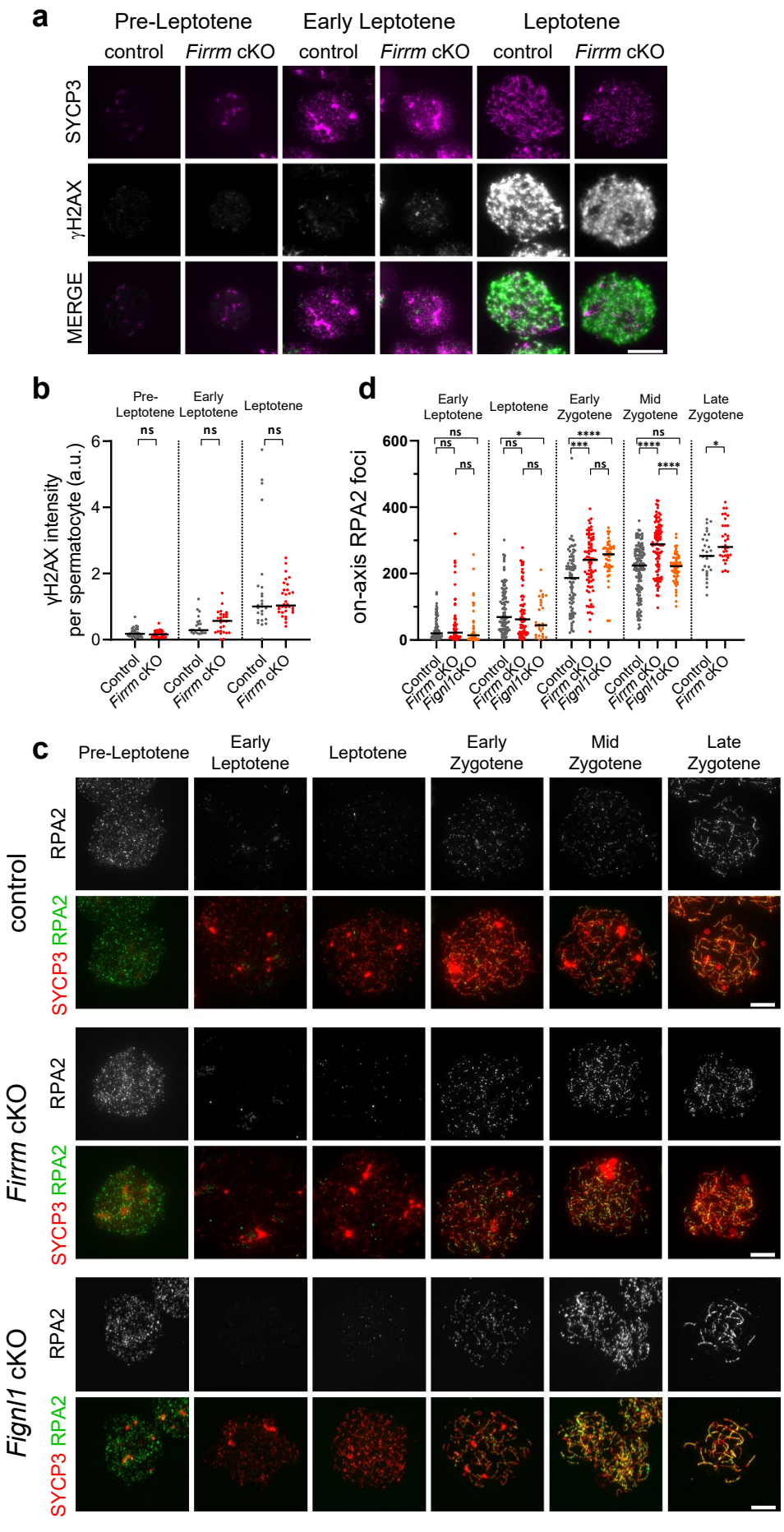
a
Pre-Leptotene
Early Leptotene
Leptotene
control
Firrm cKO
control
Firrm cKO
control
Firrm cKO
SYCP3
γH2AX
MERGE
b
Pre-Leptotene
Early Leptotene
Leptotene
γH2AX intensity per spermatocyte (a.u.)
ns
Control
Firrm cKO
d
Early Leptotene
Leptotene
Early Zygotene
Mid Zygotene
Late Zygotene
on-axis RPA2 foci
Control
Firrm cKO
Fignl1cKO
c
Pre-Leptotene
Early Leptotene
Leptotene
Early Zygotene
Mid Zygotene
Late Zygotene
control
Firrm cKO
Fignl1 cKO
RPA2
SYCP3 RPA2

Figure 3

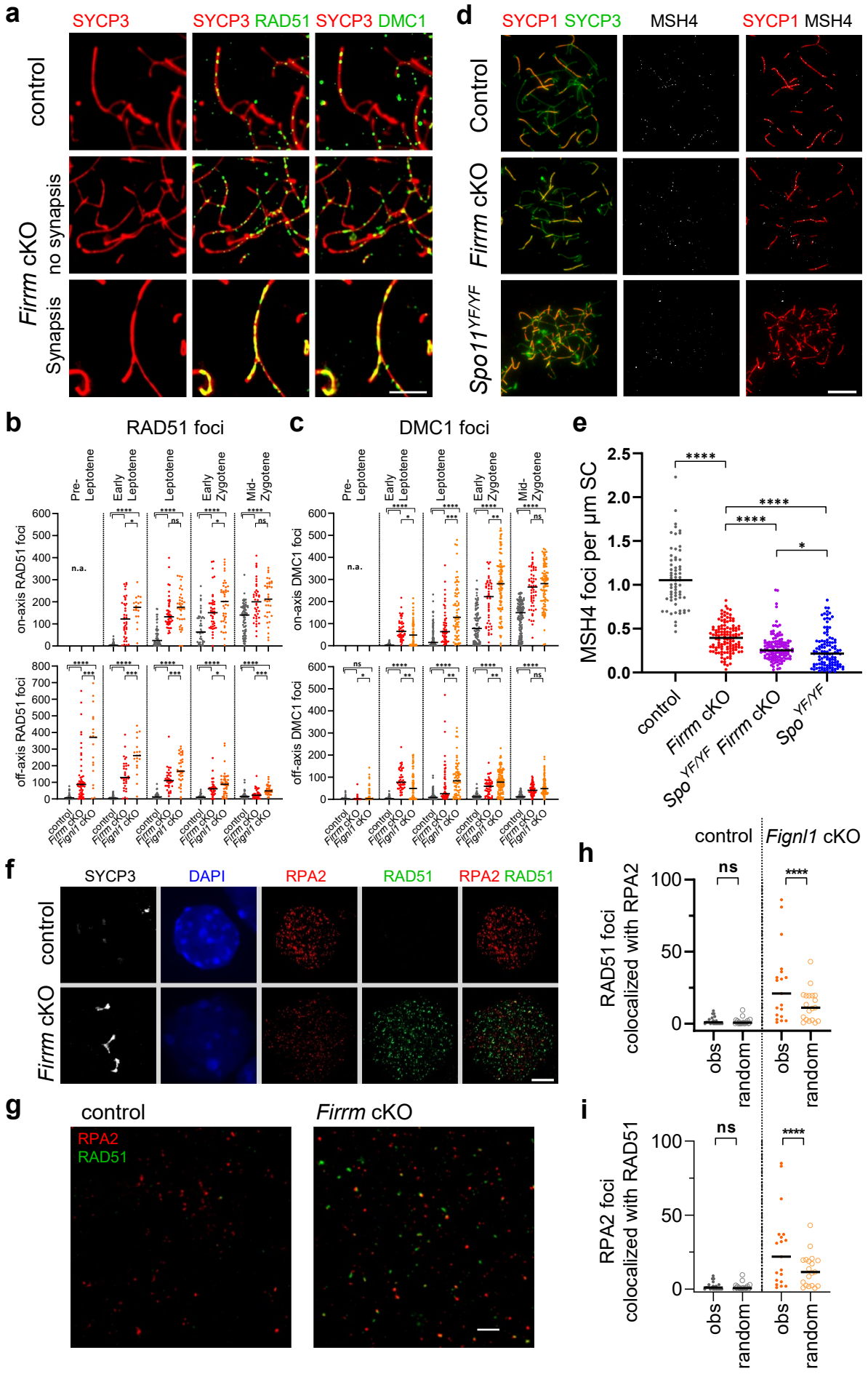
a
SYCP3
SYCP3 RAD51
SYCP3 DMC1
control
Firrm cKO
no synapsis
Synapsis
d
SYCP1 SYCP3
MSH4
SYCP1 MSH4
Control
Firrm cKO
Spo11YF/YF
b
RAD51 foci
Pre-Leptotene
Early Leptotene
Leptotene
Early Zygotene
Mid-Zygotene
on-axis RAD51 foci
off-axis RAD51 foci
n.a.
control
Firrm cKO
Fignl1 cKO
c
DMC1 foci
on-axis DMC1 foci
off-axis DMC1 foci
e
MSH4 foci per µm SC
control
Firrm cKO
Spo YF/YF
f
SYCP3
DAPI
RPA2
RAD51
RPA2 RAD51
control
Firrm cKO
g
control
Firrm cKO
RPA2
RAD51
h
control
Fignl1 cKO
RAD51 foci colocalized with RPA2
obs
random
i
RPA2 foci colocalized with RAD51

Figure 4

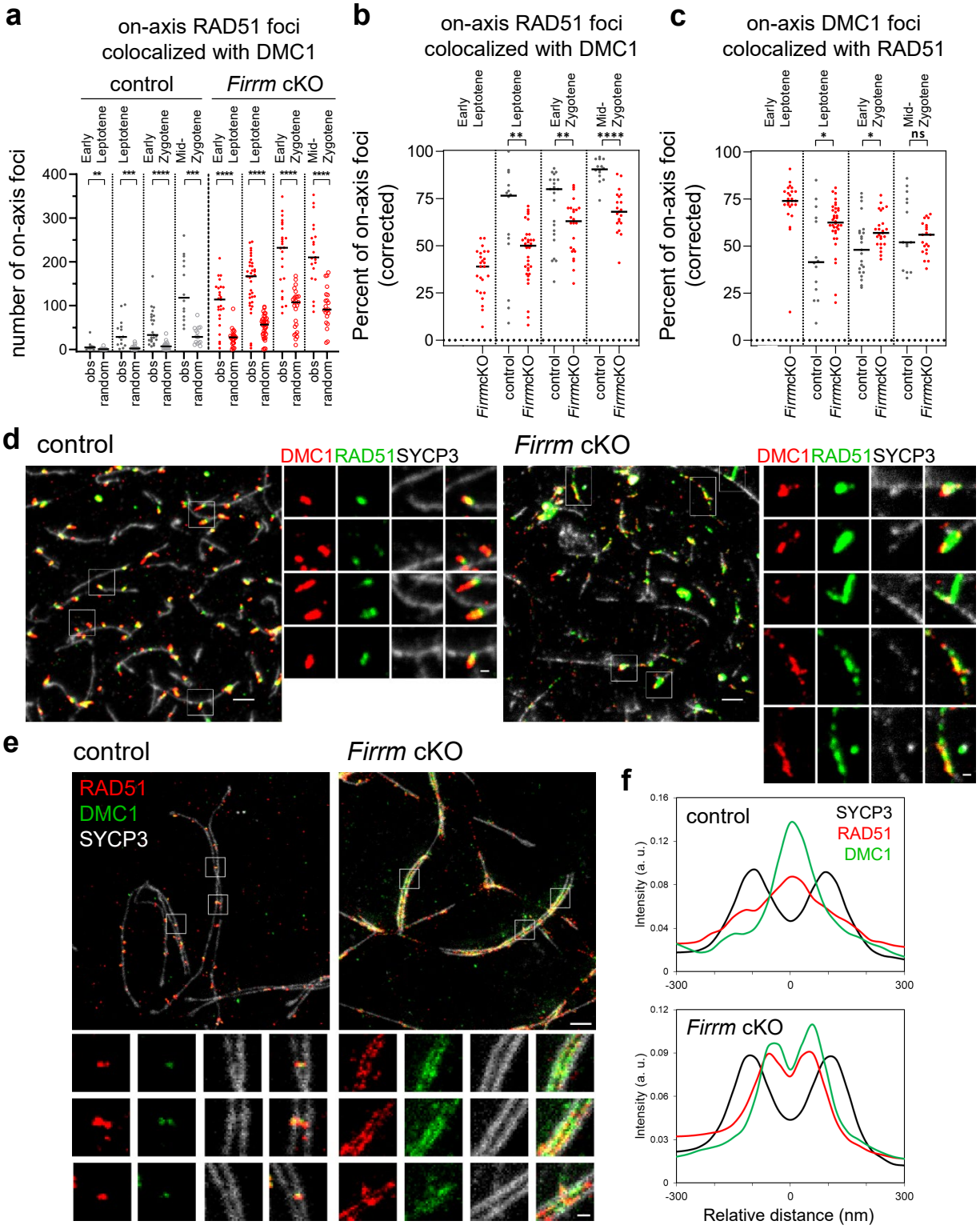
a
on-axis RAD51 foci colocalized with DMC1
control
Firrm cKO
number of on-axis foci
Early Leptotene
Leptotene
Early Zygotene
Mid-Zygotene
obs
random
b
on-axis RAD51 foci colocalized with DMC1
Percent of on-axis foci (corrected)
FirrmcKO
control
c
on-axis DMC1 foci colocalized with RAD51
Percent of on-axis foci (corrected)
ns
d
control
DMC1RAD51SYCP3
Firrm cKO
e
control
Firrm cKO
RAD51
DMC1
SYCP3
f
control
SYCP3
RAD51
DMC1
Intensity (a. u.)
Firrm cKO
Relative distance (nm)

Figure 5

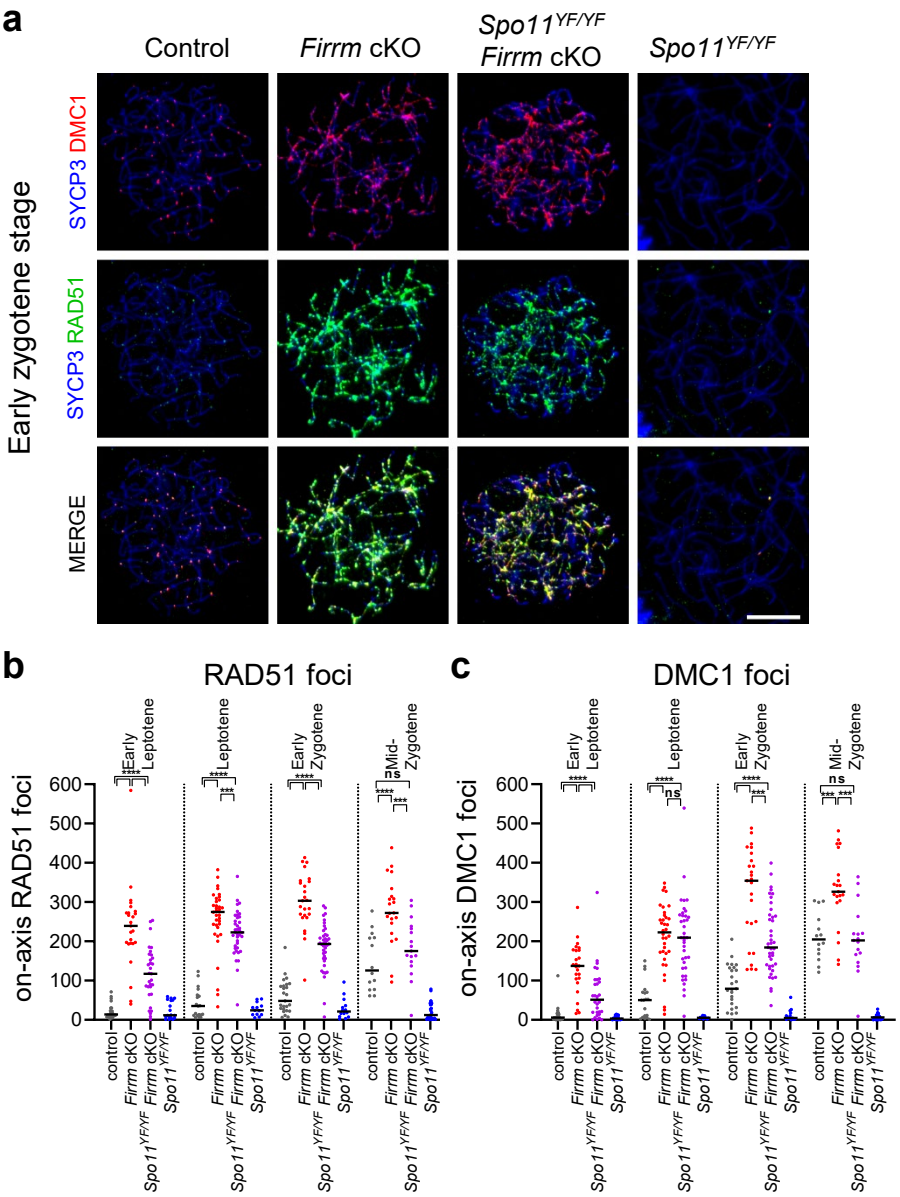
a
Control
Firrm cKO
Spo11YF/YF Firrm cKO
Spo11YF/YF
Early zygotene stage
SYCP3 DMC1
SYCP3 RAD51
MERGE
b
RAD51 foci
on-axis RAD51 foci
c
DMC1 foci
on-axis DMC1 foci
Early Leptotene
Leptotene
Early Zygotene
Mid-Zygotene
control
Firrm cKO
Spo11YF/YF Firrm cKO
Spo11YF/YF
ns

Figure 6

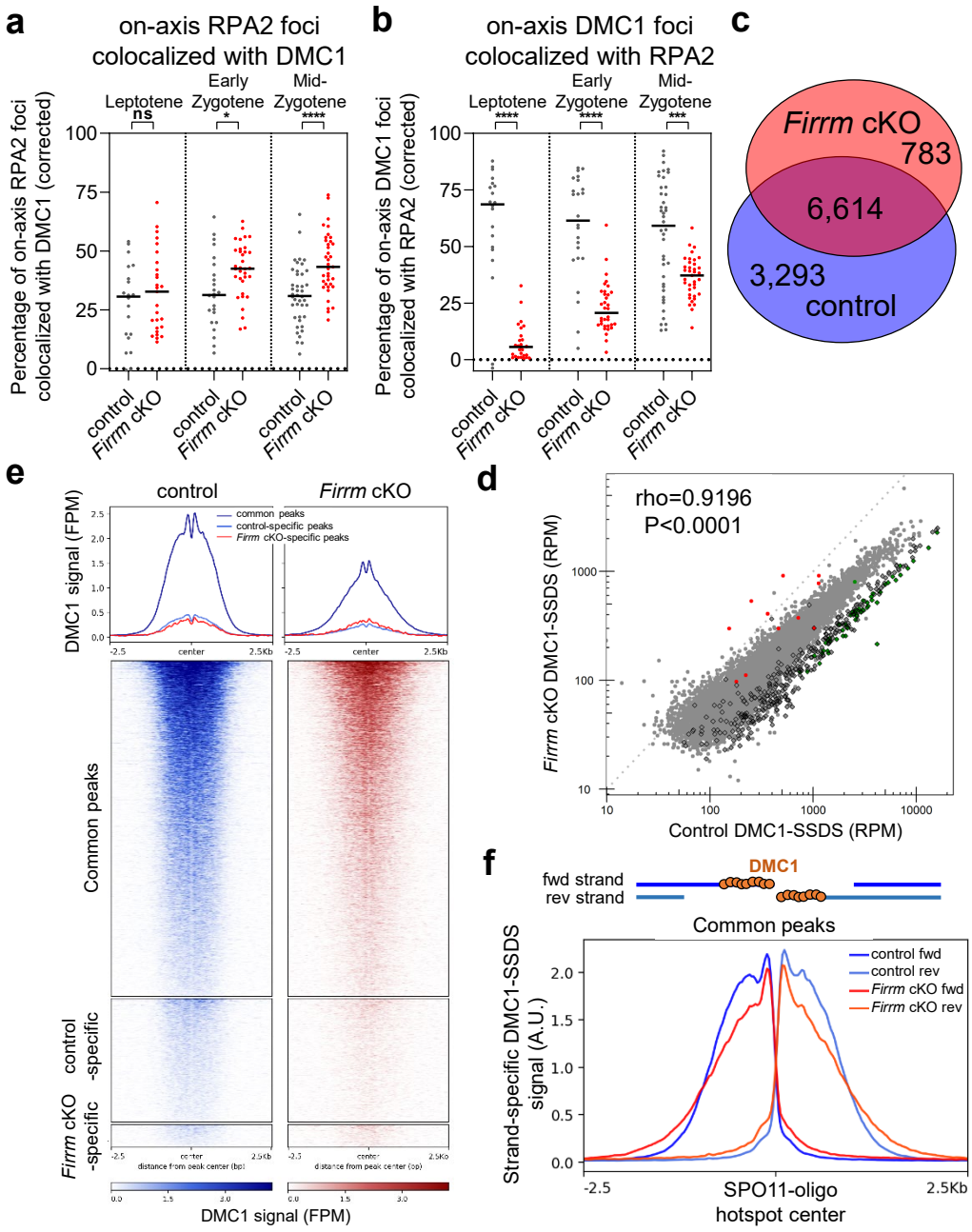
a
on-axis RPA2 foci colocalized with DMC1
Percentage of on-axis RPA2 foci colocalized with DMC1 (corrected)
Leptotene
Early Zygotene
Mid-Zygotene
ns
*
****
control
Firrm cKO
b
on-axis DMC1 foci colocalized with RPA2
Percentage of on-axis DMC1 foci colocalized with RPA2 (corrected)
****
****
***
c
Firrm cKO
783
6,614
3,293
control
e
control
Firrm cKO
DMC1 signal (FPM)
common peaks
control-specific peaks
Firrm cKO-specific peaks
Common peaks
control -specific
Firrm cKO -specific
distance from peak center (bp)
DMC1 signal (FPM)
d
rho=0.9196
P<0.0001
Firrm cKO DMC1-SSDS (RPM)
Control DMC1-SSDS (RPM)
f
DMC1
fwd strand
rev strand
Common peaks
control fwd
control rev
Firrm cKO fwd
Firrm cKO rev
Strand-specific DMC1-SSDS signal (A.U.)
SPO11-oligo hotspot center

Figure 7

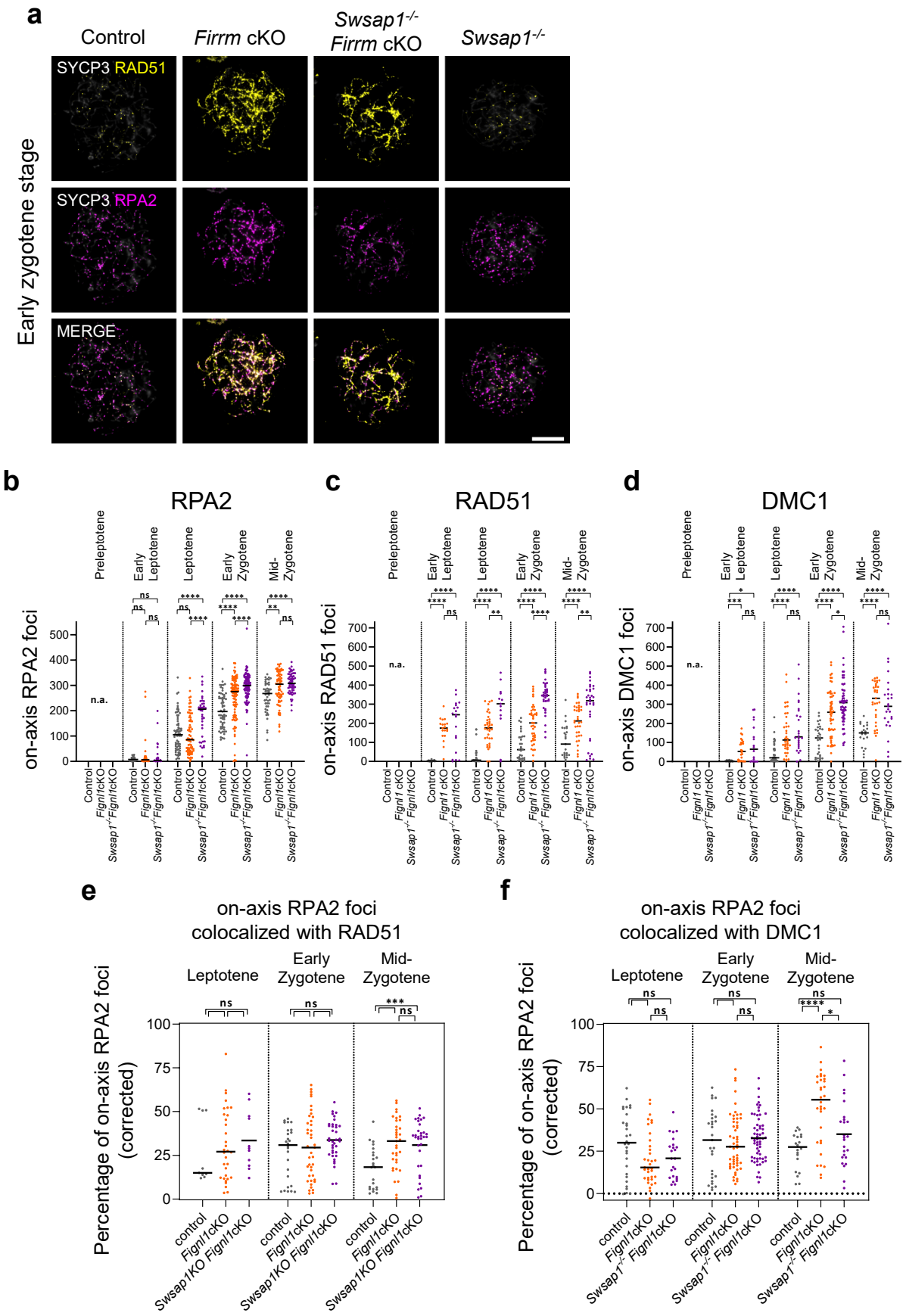
a
Control
Firrm cKO
Swsap1-/- Firrm cKO
Swsap1-/-
Early zygotene stage
SYCP3 RAD51
SYCP3 RPA2
MERGE
b
RPA2
on-axis RPA2 foci
c
RAD51
on-axis RAD51 foci
d
DMC1
on-axis DMC1 foci
Preleptotene
Early Leptotene
Leptotene
Early Zygotene
Mid-Zygotene
n.a.
Control
Figni1cKO
Swsap1-/- Figni1cKO
e
on-axis RPA2 foci colocalized with RAD51
Percentage of on-axis RPA2 foci (corrected)
Leptotene
Early Zygotene
Mid-Zygotene
control
Figni1cKO
Swsap1KO Figni1cKO
f
on-axis RPA2 foci colocalized with DMC1
Swsap1-/- Figni1cKO

Figure 8

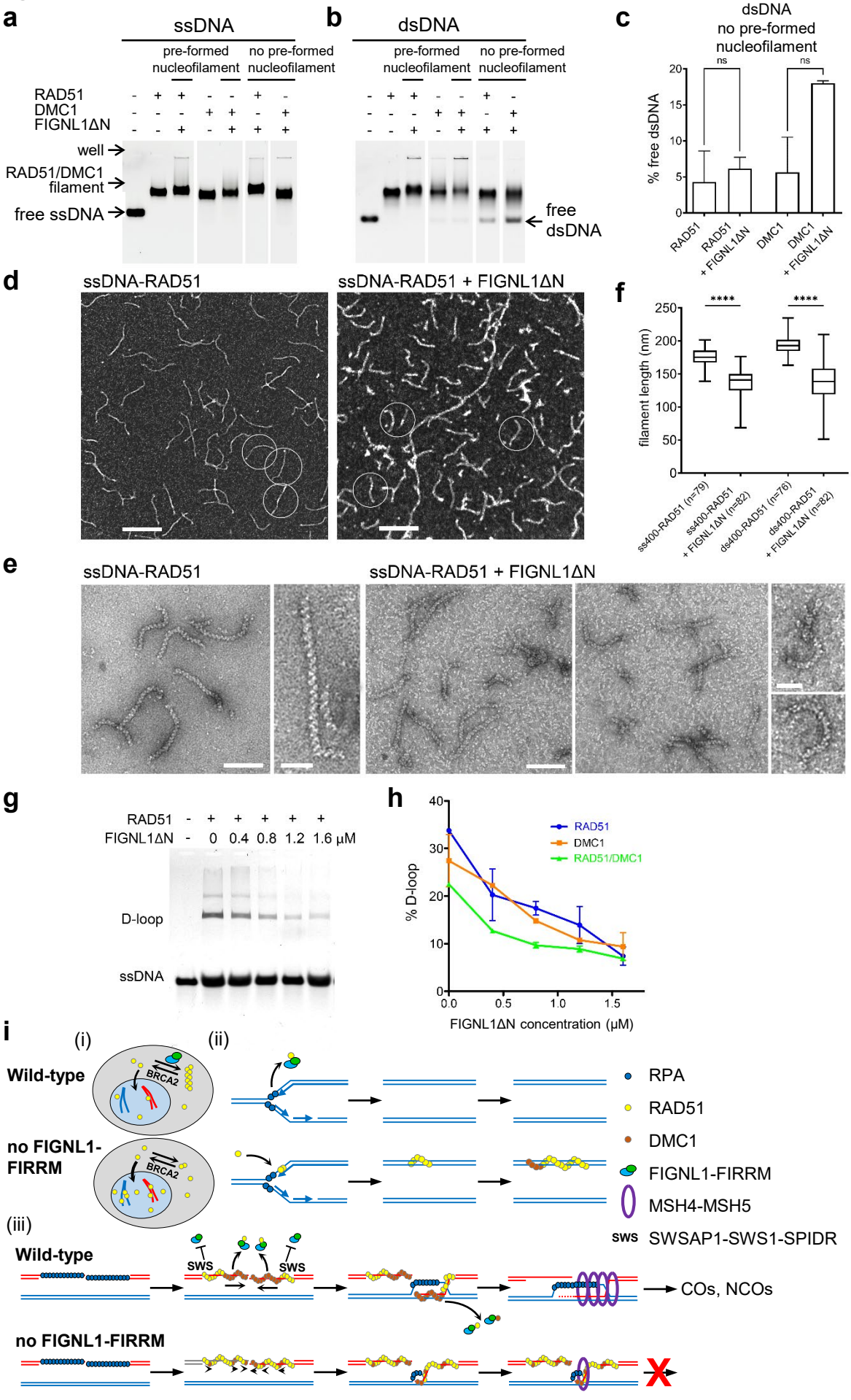
a
ssDNA
pre-formed nucleofilament
no pre-formed nucleofilament
RAD51
DMC1
FIGNL1ΔN
well
RAD51/DMC1 filament
free ssDNA
b
dsDNA
pre-formed nucleofilament
no pre-formed nucleofilament
free dsDNA
c
dsDNA
no pre-formed nucleofilament
ns
ns
% free dsDNA
RAD51
RAD51 + FIGNL1ΔN
DMC1
DMC1 + FIGNL1ΔN
d
ssDNA-RAD51
ssDNA-RAD51 + FIGNL1ΔN
f
****
****
filament length (nm)
ss400-RAD51 (n=79)
ss400-RAD51 + FIGNL1ΔN (n=82)
ds400-RAD51 (n=76)
ds400-RAD51 + FIGNL1ΔN (n=82)
e
ssDNA-RAD51
ssDNA-RAD51 + FIGNL1ΔN
g
RAD51
FIGNL1ΔN 0 0.4 0.8 1.2 1.6 μM
D-loop
ssDNA
h
RAD51
DMC1
RAD51/DMC1
% D-loop
FIGNL1ΔN concentration (μM)
i
(i)
(ii)
Wild-type
BRCA2
no FIGNL1-FIRRM
BRCA2
(iii)
Wild-type
SWS
SWS
COs, NCOs
no FIGNL1-FIRRM
RPA
RAD51
DMC1
FIGNL1-FIRRM
MSH4-MSH5
SWS SWSAP1-SWS1-SPIDR

Extended Data Figure 1

a

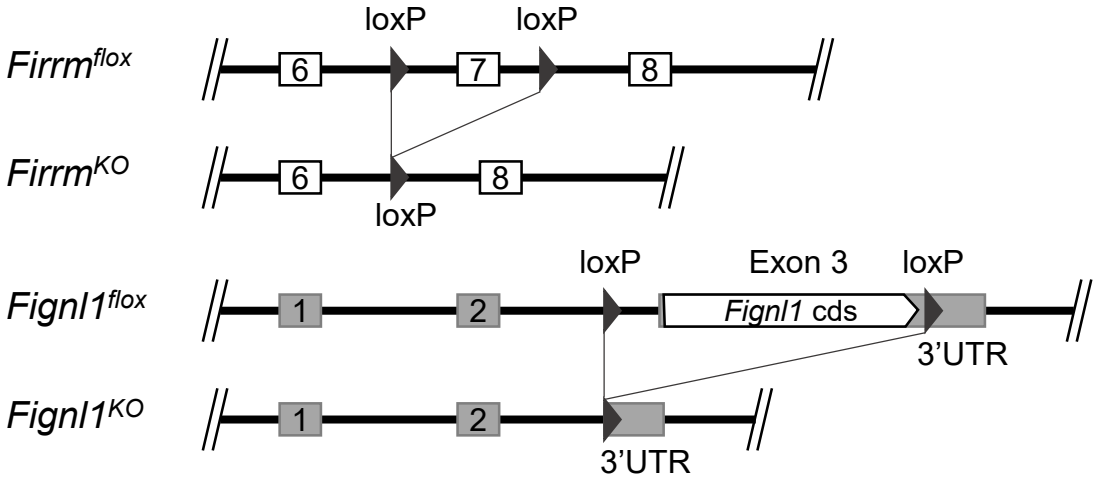

b

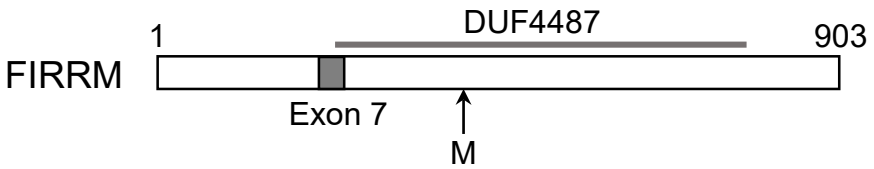

Extended Data Figure 2

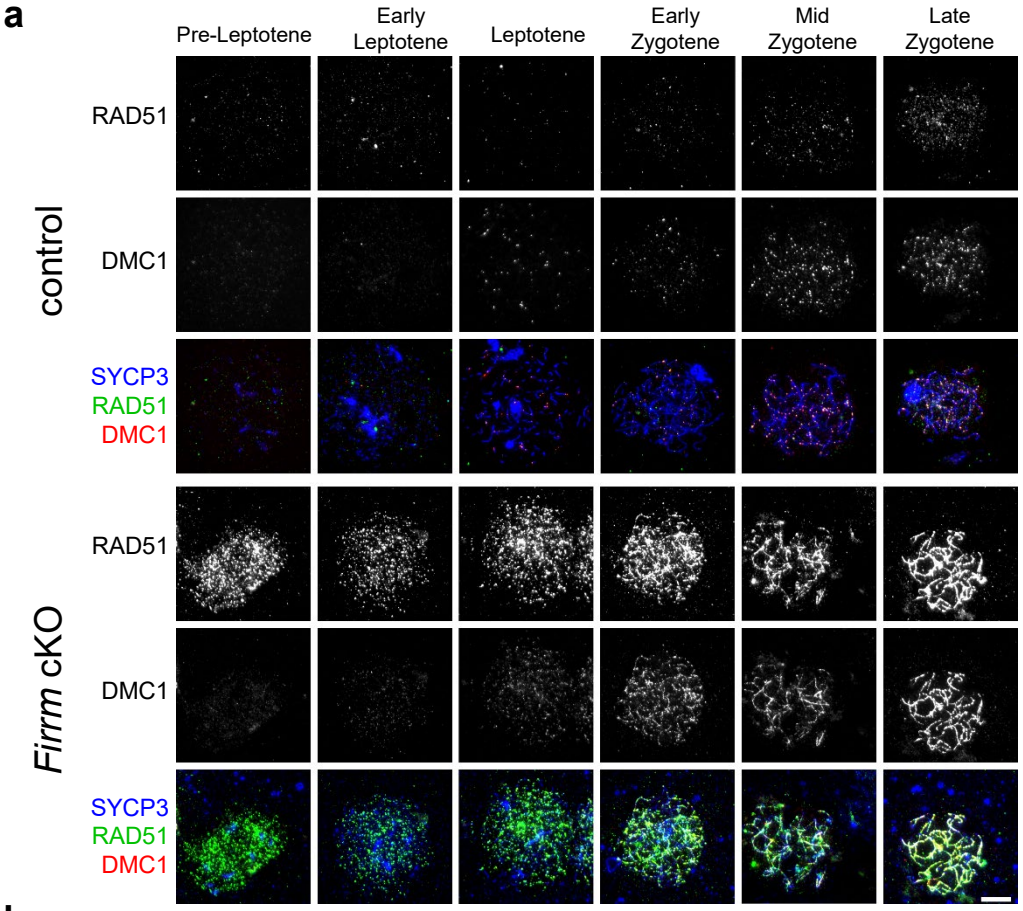

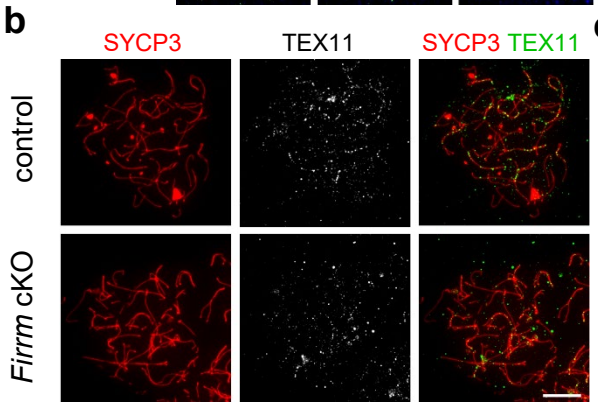

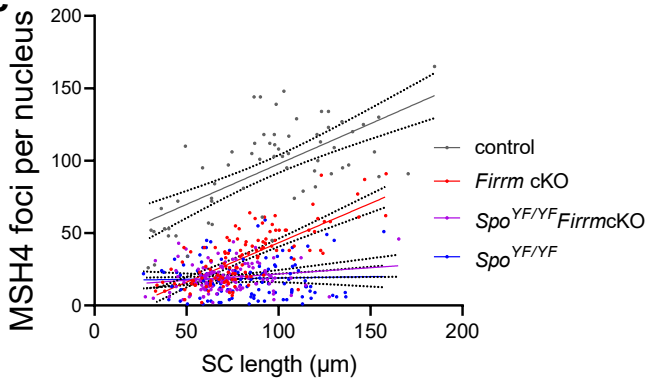

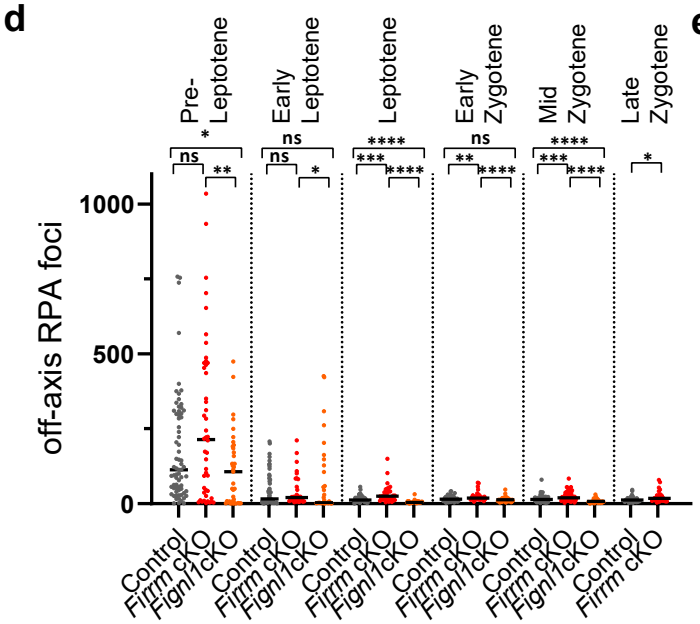

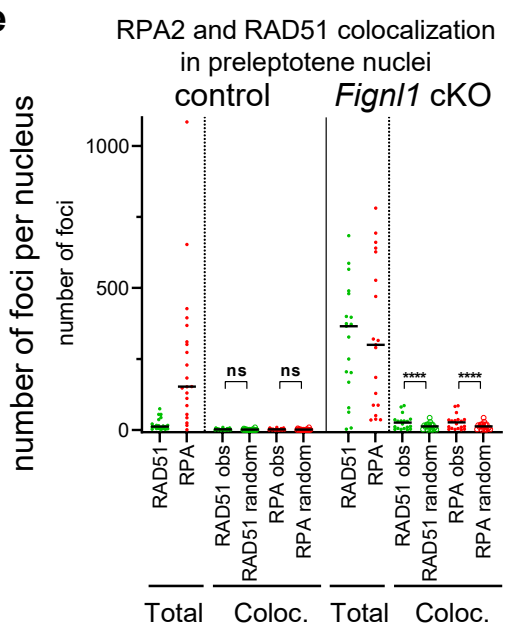

Extended Data Figure 3

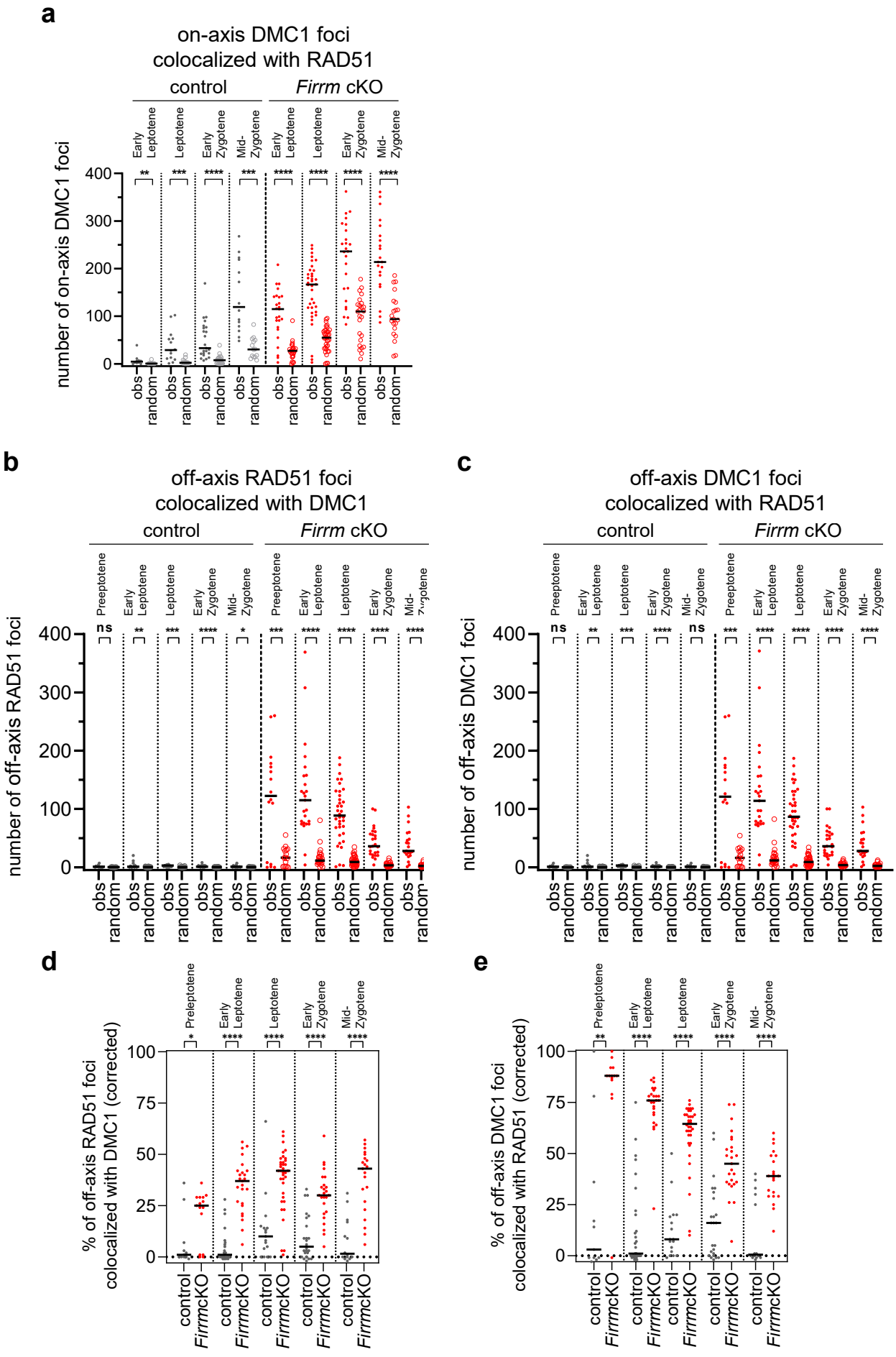

Extended Data Figure 4

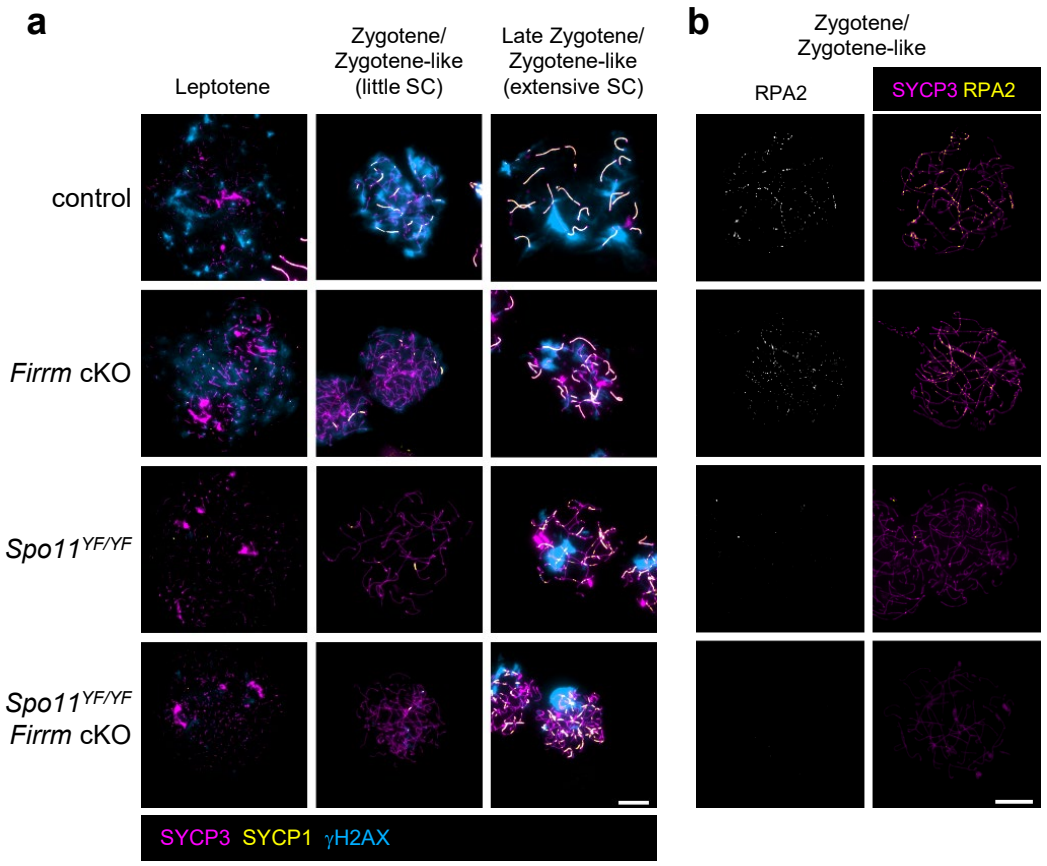

Extended Data Figure 5

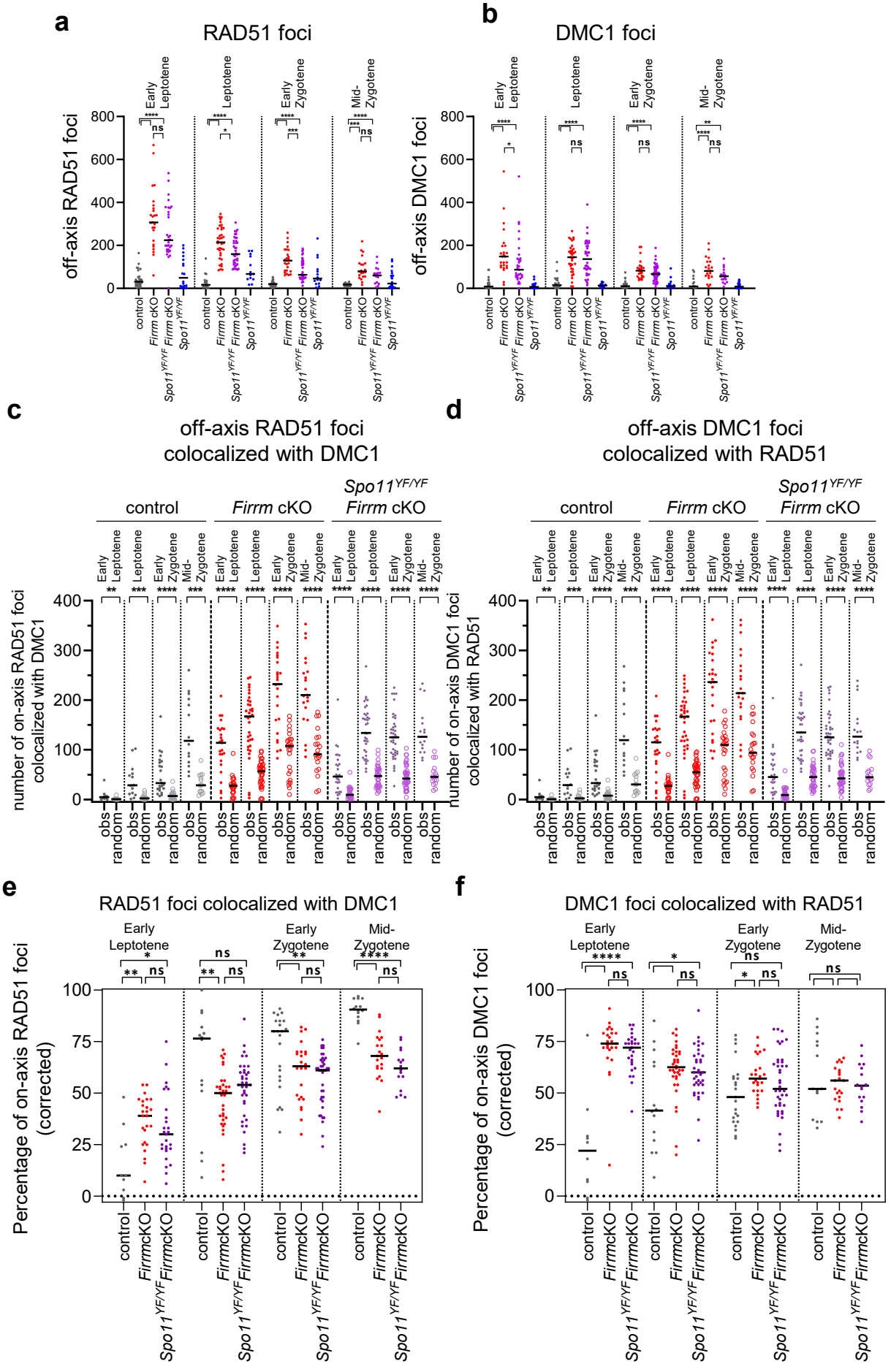

Extended Data Figure 6

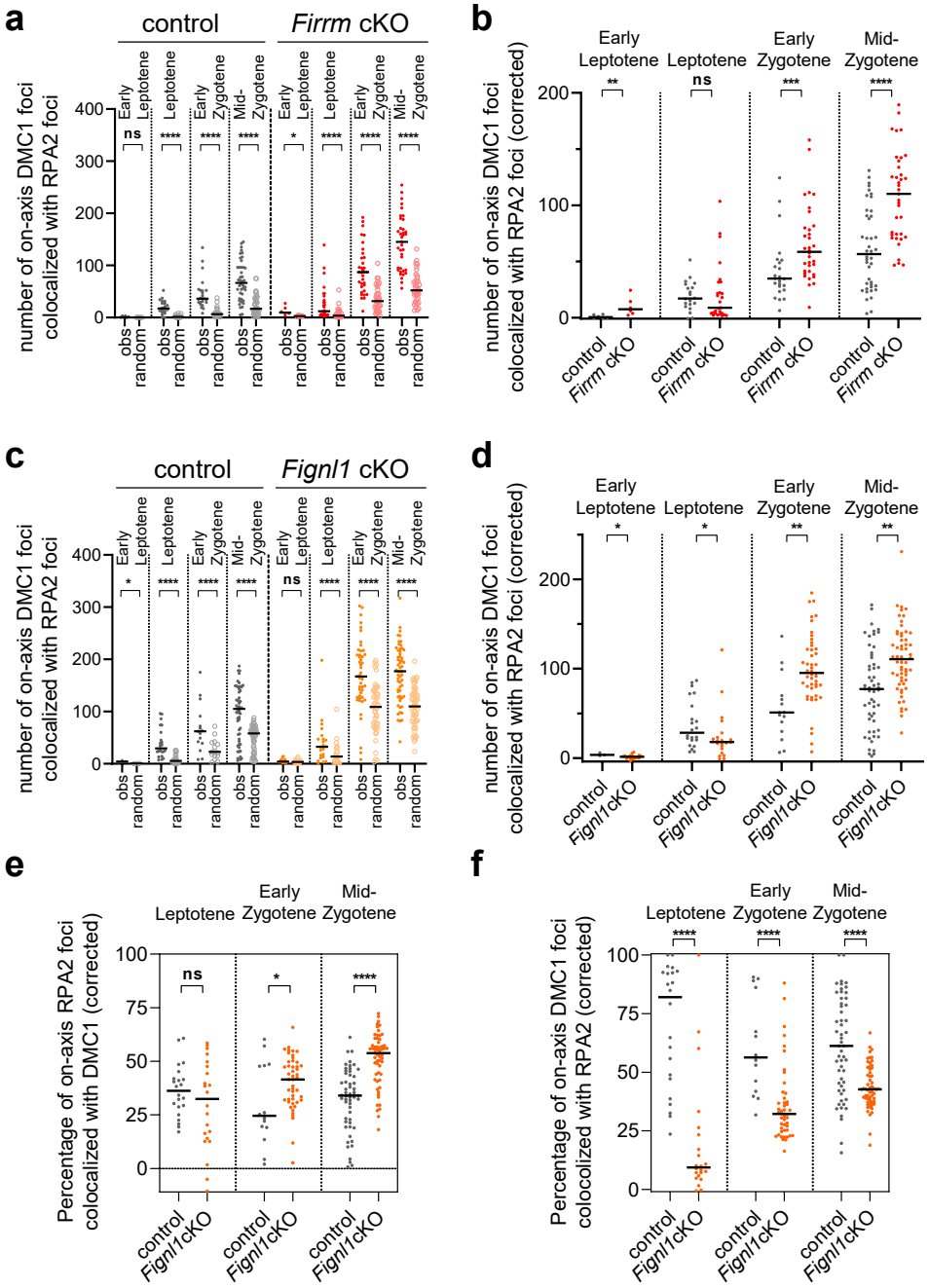

Extended Data Figure 7

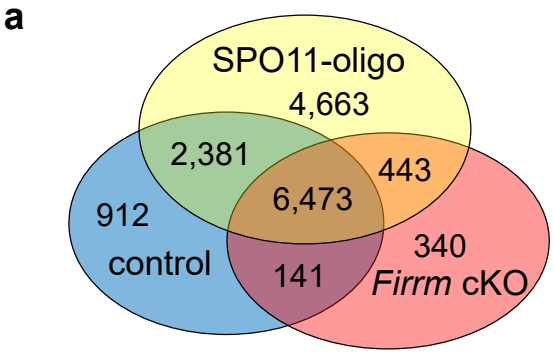

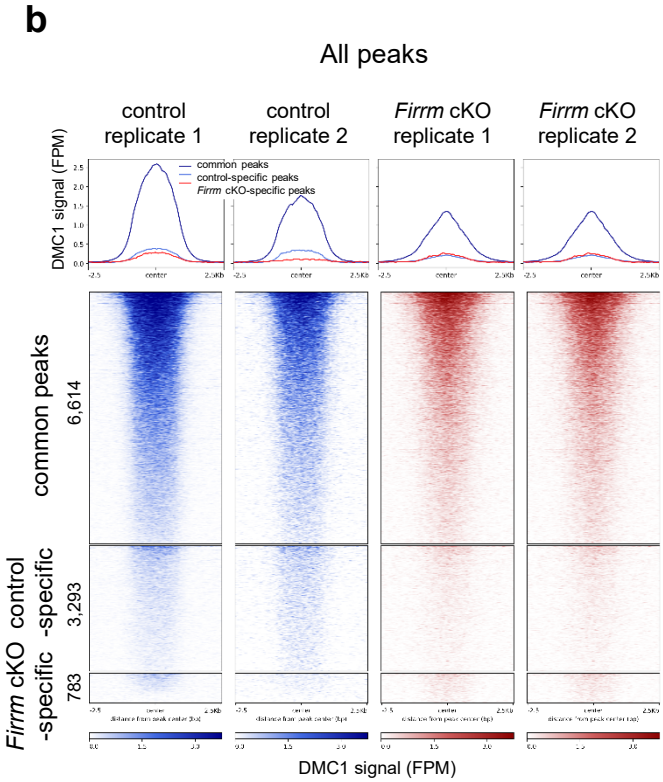

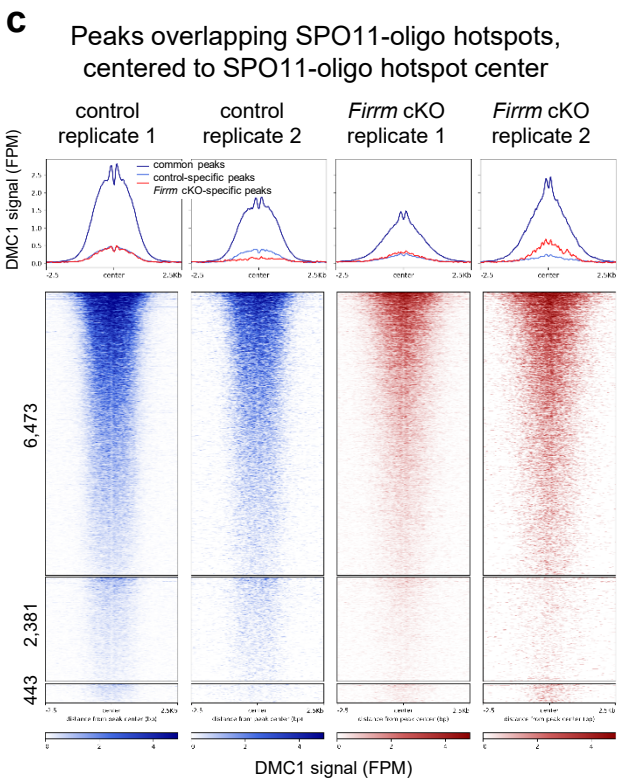

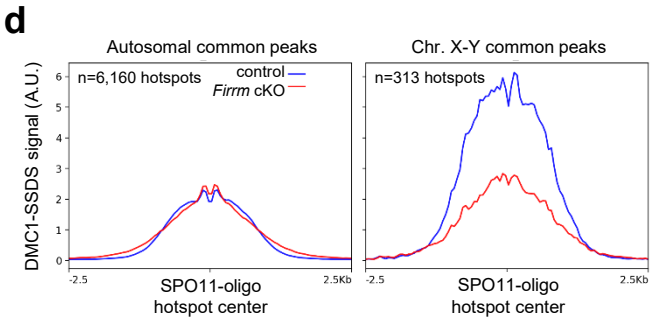

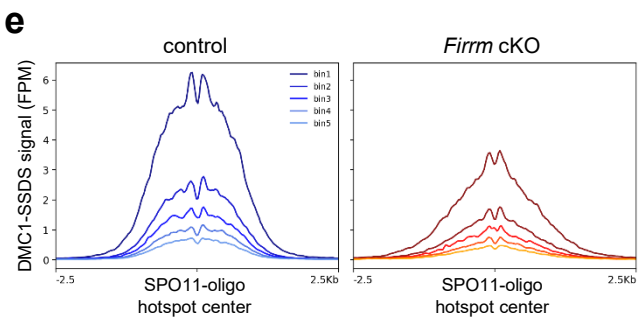

Extended Data Figure 8

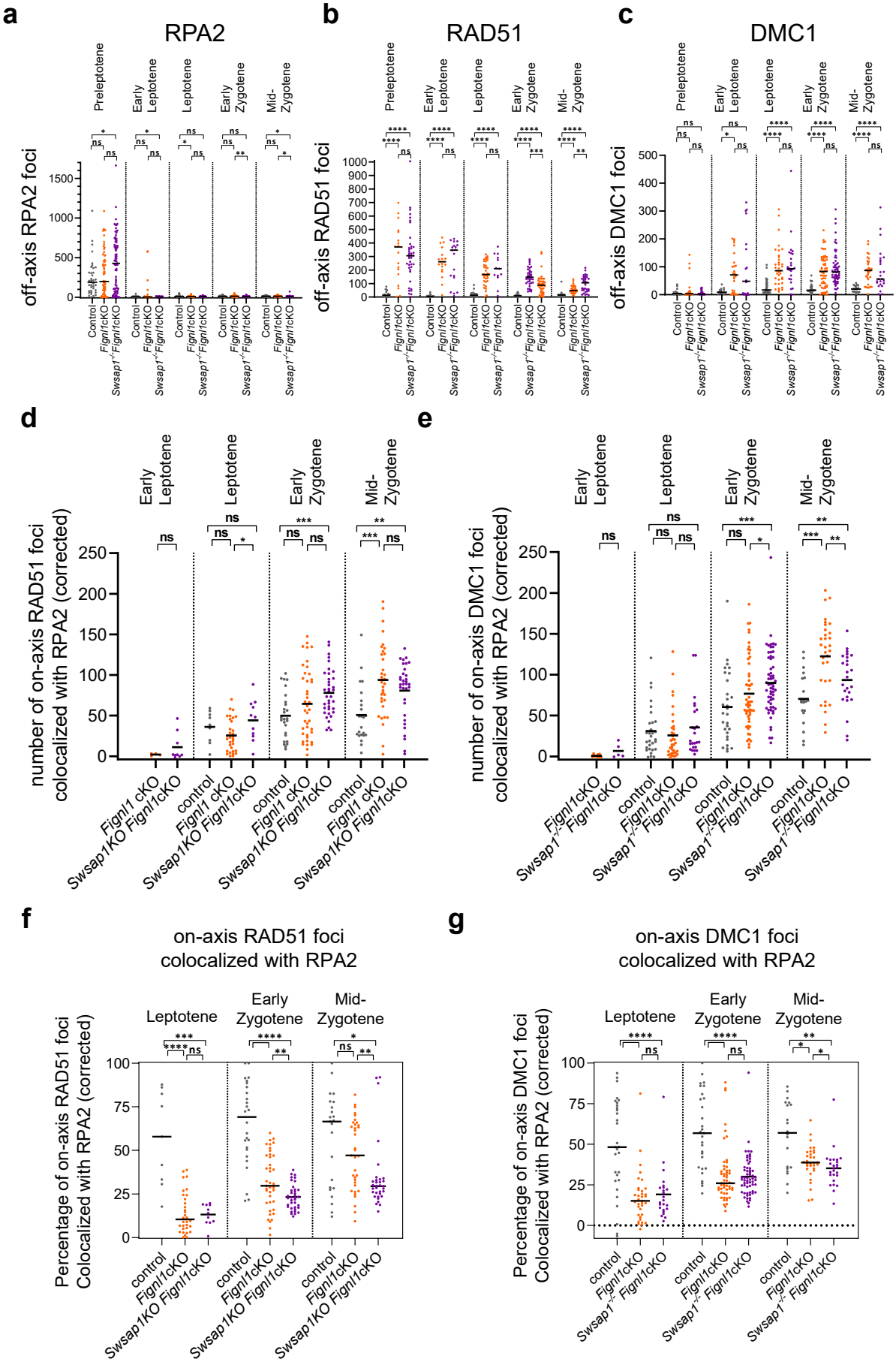

Extended Data Figure 9

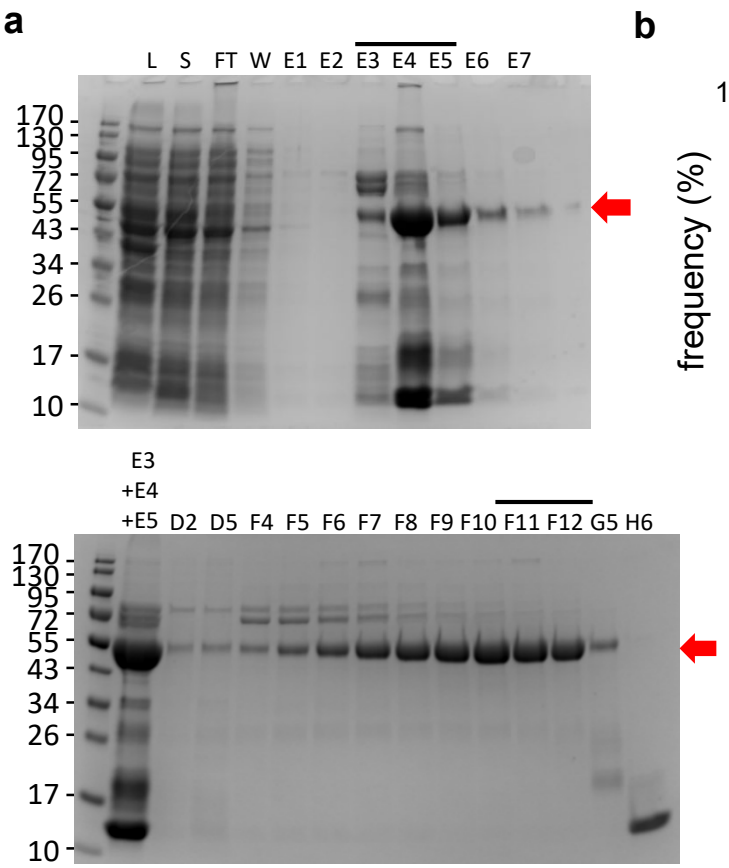

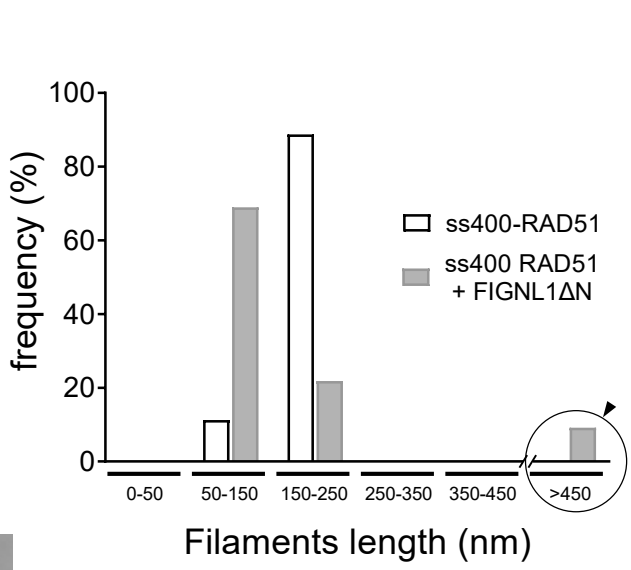

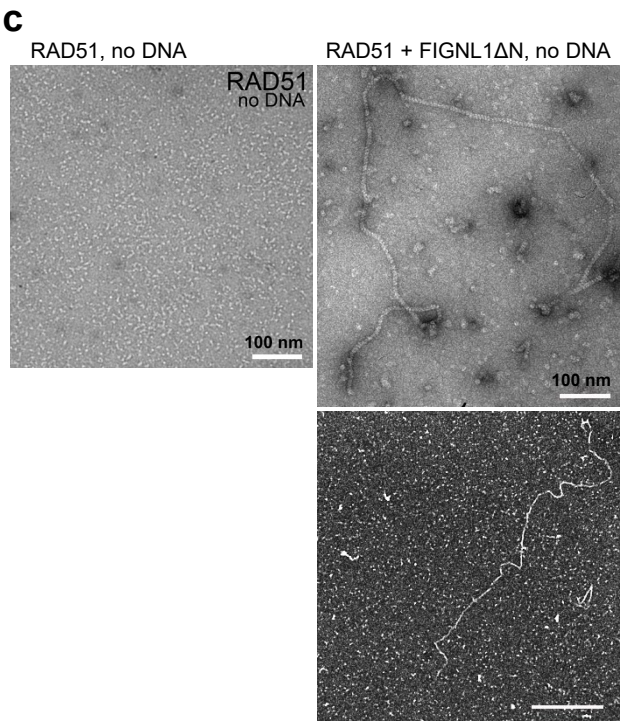

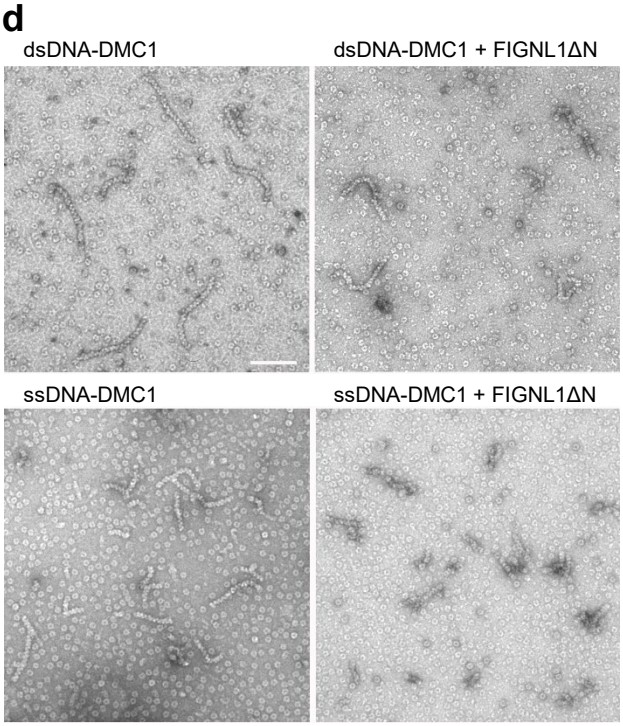

Source Data

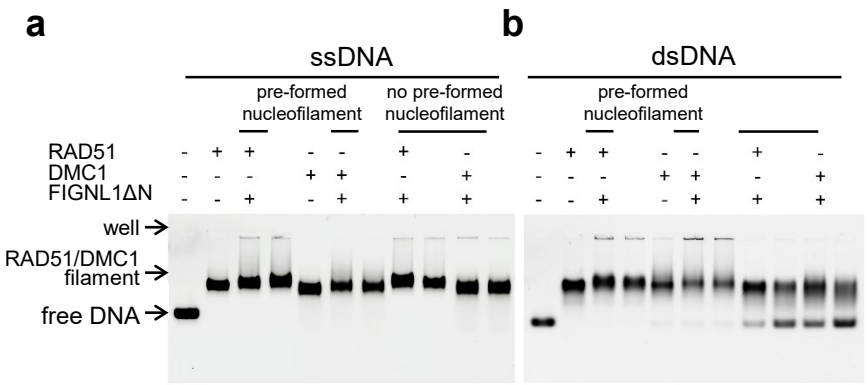
a
b
ssDNA
dsDNA
pre-formed nucleofilament
no pre-formed nucleofilament
pre-formed nucleofilament
RAD51
DMC1
FIGNL1ΔN
well
RAD51/DMC1 filament
free DNA